Evaluation of Hyperspectral Snapshot Imagers onboard Nanosatellite Clusters for Multi-Angular Remote Sensing

Sreeja Nag[1], Kerri Cahoy[2], Olivier de Weck[3]
Massachusetts Institute of Technology, Cambridge, MA 02139

Charles K. Gatebe[4], Georgi Georgiev[5], Tilak Hewagama[6], Shahid Aslam[7], Bert Pasquale[8]
NASA Goddard Space Flight Center, Greenbelt, MD 20771

Hyperspectral snapshot imagers are capable of producing 2D spatial images with a single exposure at selected and numerous wavelength bands instead of 1D spatial at all spectral band images like in push-broom instruments. Snapshot imagers are critical technologies for multi-angle remote sensing using distributed space missions. They help to relax the attitude control requirements of clusters of small satellites whose narrow field-of-view payloads point at the same ground spot or to increase the footprint area of small satellite constellations with wide field-of-view payloads. This paper reviews the existing spectral imagers for multi-angle remote sensing, performs a feasibility study to incorporate existing state-of-the-art snapshot imagers and proposes baseline imagers to serve as payload for the distributed nanosatellites. The overall approach includes an extensive trade study to identify the optics, spectral elements, their parameters and compare the identified choices both qualitatively and quantitatively. The proposed baseline design has an telescope aperture diameter of 7 cm, focal plane pixel size of 20 μm, 1000 pixels per side of the focal plane array sampling the scene and acousto-optic tunable filters or waveguide spatial heterodyne imagers that simulate a swath up to 90 km, image up to 86 wavebands with an SNR above 100. The trade-off between spectral and spatial ranges sampled by the two baseline imager options has been highlighted.

I. Introduction

Multi-angle, multi-spectral remote sensing is very important for many earth science remote sensing applications, e.g. derivation of surface albedo[1], calculation of radiative forcing[2], land cover classification[3], cloud detection[4], atmospheric corrections, and aerosol optical properties[5]. Bidirectional reflectance-distribution function (BRDF) is a basic parameter for describing (geometrically) the reflecting properties of a surface element, and depends on 3D geometry of incident and reflected elementary beams[6]. Fully characterized BRDF measurements have broad application in earth science fields including climate and energy budget. Satellite clusters in formation flight with narrow field-of-view (NFOV) imagers or satellite constellations with wide field-of-view (WFOV) imagers are currently being evaluated as an efficient method of sampling the BRDF function in all five dimensions – angular, temporal, spatial, spectral, and radiometric. To evaluate the feasibility of this concept and identify a baseline mission architecture, a systems engineering (SE) model integrated with traditional BRDF estimation models is being developed for tradespace exploration and optimization[7]. The SE model contains the following critical modules: global orbits and formation flight cluster geometry, guidance navigation and control systems, communication, payload and complexity evaluation. The payloads will be Visible and Near Infra-Red (VNIR) snapshot imagers as BRDF is estimated at near solar insolation wavelengths. This paper concentrates on the payload modeling, which is the key driver for the spatial, spectral, and radiometric sampling of the BRDF function and thus multi-angle remote

---

[1] Graduate Research Fellow, Department of Aeronautics and Astronautics, MIT and AIAA Student Member

[2] Assistant Professor, Department of Aeronautics and Astronautics and Earth, Atmospheric and Planetary Science, MIT

[3] Professor, Department of Aeronautics and Astronautics and Engineering Systems Division, MIT and AIAA Associate Fellow

[4] Associate Research Scientist, Climate and Radiation Branch, NASA GSFC and Universities Space Research Association

[5] Instrument Engineer, Climate and Radiation Branch, NASA GSFC and Sigma Space Corp.

[6] Research Scientist, University of Maryland, College Park and Solar System Exploration Division, NASA GSFC.

[7] Associate Planetary Scientist, Solar System Exploration Division, NASA GSFC

[8] Research Physicist, Optics Branch, NASA GSFC

sensing applications to earth science. The technical feasibility of developing a payload using commercial-off-the-shelf components and existing spectrometer technologies that can achieve BRDF science has been evaluated and a potential baseline for an NFOV instrument proposed.

A. Existing Multi-Angle, Multi-Spectral Instruments

Many current and past missions have performed multi-angle, multi-spectral Earth observations by use of a monolithic platform and instrument. To capture all the important optical features necessary for describing different surface types, a BRDF-oriented space mission[8] requires radiance measurements across a large angular spread of both solar illumination and detector directions, fine spatial resolution, frequent repeat of the ground track for a high temporal resolution and measurements across multiple wavelengths - large spectral range, high spectral resolution in the visible and near infrared (VNIR) solar spectrum and sometimes polarization state. Trade-offs between the variables depend on geoscience applications where the theoretical BRDF is used.

All spaceborne instruments provide sparse sampling of the BRDF function. These instruments estimate BRDF by making multi-angular measurements owing to their large cross track swath (e.g. Moderate Resolution Imaging Spectroradiometer-MODIS[9], Polarization and Directionality of the Earth's Reflectances-POLDER[10], Clouds and Earth's Radiant Energy System-CERES[11]), multiple forward and aft sensors (e.g. Multi-angle Imaging SpectroRadiometer-MISR[12], Along Track Scanning Radiometer-ATSR[13], Advanced Spaceborne Thermal Emission and Reflection Radiometer-ASTER[14]), or autonomous maneuverability to point at specific ground targets that they have been commanded to observe (e.g. Compact High Resolution Imaging Spectrometer -CHRIS[15]). But all the instruments fall short in at least one major BRDF sampling dimension mentioned in the previous section. POLDER, CERES have very coarse ground resolution, therefore BRDF estimates are applicable to only large spatial scales. MISR and CHRIS have a small spectral range and exclude BRDF information on short wave infrared (SWIR). CHRIS has no target repeatability to capture BRDF's temporal change. Since full BRDF sampling requires simultaneous reflectance measurements at multiple angles for a given ground footprint, one satellite is insufficient for accurate characterization. A single satellite can make measurements only along a restrictive plane with respect to the solar phase. Most EOS satellites are even more restricted since they are locked in sun-synchronous orbits. Further, the angular measurements are separated in time by many minutes along-track (e.g. MISR) or weeks cross-track (e.g. MODIS). In areas of fast changing surface/cloud conditions, especially during the snow melt season/tropical storms, a few days can make a big difference in reflectance. All instruments that depend on large swaths have no azimuthal coverage on the 3D angular sampling plane within a few hours because angular data is obtained by the overlap of measurements taken in consecutive orbits. Angular data collected by instruments dependent on multiple sensors are limited by the number of sensors. Finally, all the current BRDF instruments are nearing end of life and with the lack of a morning orbit in the JPSS-era, there will be a temporal gap in global BRDF measurements.

Airborne instruments can maximize fulfilling all science metrics except global coverage and repeatability. It is extremely expensive, if at all possible, to achieve global coverage with regular temporal repeats using aircrafts. NASA's heritage airborne BRDF instrument is called the Cloud Absorption Radiometer (CAR), developed at Goddard Space Flight Center (GSFC), has 14 channels of binwidth 6-40 nm, makes up to 114600 directional measurements of radiance per channel per aircraft circle at a spatial resolution of 10-270 m but samples select geographic locations over a few hours[5].

B. Requirement of Distributed Space Missions with Hyperspectral Snapshot Imagers

The past two decades have seen the conceptual development of distributed space systems (DSS) from homogenous constellations such as GPS and Iridium to fractionated spacecraft such as F6[16] and associated technologies such as formation flight, scatter maneuvers[17], high data rate communication links[18] and open-source cluster flight development[19–22]. A possible solution to BRDF sampling is the use of a DSS of nanosatellites (<10 kg) on a repeating-ground-track orbit. DSS can make multi-spectral measurements of a ground spot at multiple 3D angles at the same time as they pass overhead either using NFOV instruments in controlled formation flight (Figure 1-left) or WFOV instruments with overlapping ground spots imaged at different angles flight (Figure 1-right). Many nanosatellites can be deployed for the resources, quantified especially by cost, of a current large monolith[23]. Nanosatellites currently come in standardized formats, easy to build, customize and launch. For example, the 6U cubesat is a standard satellite bus ideal for university programs and is currently the largest for launch on the Poly-PicoSatellite Orbital Deployer.

Small VNIR spectrometers are required as payload on the nanosatellites, customized to sample the BRDF function as required. The pointing requirements for a mission with NFOV instruments are relatively strict because all the satellites have to point their NFOV payload toward the same ground spot at the same time for the multi-angle image to be correctly registered. If push broom sensors are used, only a single row of pixels will be available in the zenith angular direction and an error equal to the instantaneous field of view (iFOV) would lead to the loss of one angular measurement. For example, if the iFOV is 0.1^o, then a satellite's zenith error of 0.1^o will cause that satellite to miss the common ground target. This pointing risk may be avoided by the use of hyperspectral snapshot imaging (HSI) which produces 2D spatial images with a single exposure at selected and numerous wavelength bands. HSI is also required if constellations of WFOV satellites are flown such that multi-angle images of any ground spot are generated by co-registering the 3D images from all the satellites in view of the spot because circular or rectangular spots increase the area and instances of overlap. The WFOV approach is a constellation approach to the POLDER instrument and coarsens the spatial resolution of the measurements. Small hyperspectral snapshot imagers for nanosatellites have never been developed, calling for a systems-based approach in designing them and evaluating their feasibility.
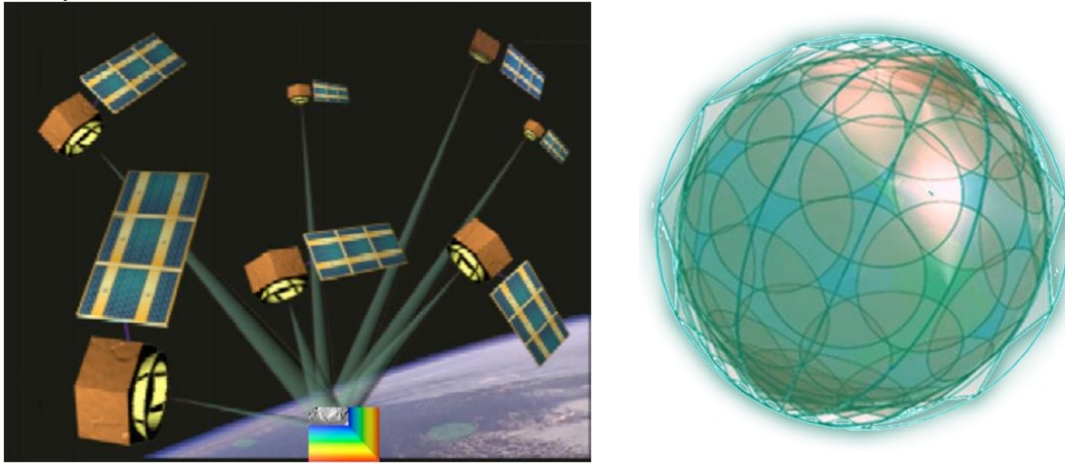

Figure 1: [Left] A DSS making multi-angular, multi-spectral measurements by virtue of pointing its NFOVs at the same ground spot, as it orbits the Earth as a single system (adapted from Leonardo BRDF[4]). [Right] A DSS making multi-angular, multi-spectral measurements by virtue of their overlapping WFOVs at different angles (from GEOScan[24]).

C. Small Satellite Spectrometers

Existing spectrometers and spectro-radiometers for MA observations have traditionally been very large. MODIS is 228.7 kg and MISR is 148 kg. CHRIS is the lightest instrument among the ones listed in Section IB, at 14 kg. Therefore, significant amount of development needs to be done to reduce the spectrometer mass while adding the additional requirement of 3D (2D spatial and 1D spectral) images. The radiometric precision, image quality and signal to noise ratios (SNR) of the small satellite images are not expected to be similar to the heritage instruments such as MODIS and MISR however, the images are required to have SNR enough to distinguish signals captured by different satellites at different 3D angles so that co-registration provides an accurate relative MA image. These observations may then be used complimentarily with high quality data from heritage missions, and thus provide a data dimension (angular) that has never been captured before.

Hyperspectral snapshot imagers make measurements as a 3D data cube, as required, but have never been demonstrated on nanosatellites. Theoretically popular methods for imaging are computerized tomography to calculate the 3D input (x,y,λ) from the 2D output image on the Focal Plane Array (FPA) at multiple diffraction orders[25,26], image slicers made of appropriately aligned mirrors and grisms to slice the 2D spatial image into a 1D vector and then disperse it spectrally[27], multiple apertures at the input lens[28] followed by a dispersive or a spectral element such as a Fabry-Perot filter array[29] and birefringent interferometers for spectral filtering by two-beam interference followed by spatial/spectral demultiplexing by passing the light through a Wollaston prism[30]. All the above designs showed an apparent trade-off between size, resolution and numerical singularities. Tomographic approaches suffer from typical problems of inverse solutions, image slicers need cryogenic temperatures (although the modern version of the Bowen slicer has demonstrated otherwise) and fiber optic reformatters are preferred at visible and NIR wavelengths[31] and multiple apertures severely restrict the spatial FOV and thus ground resolution.

Many hyperspectral technologies have been based on the concept of wavelength tunable filters[32]. Liquid Crystal Tunable Filters (LCTF) have been used in several Hyperspectral Imager Systems (HIS). A Lyot-Ohman type LCTF which consists of a stack of polarizers and tunable retardation (birefringent) liquid crystal plates has been used in many hyperspectral imaging instruments in the VNIR wavelength range. Liquid crystals however are limited by the relaxation time of the crystal and is in the range of 40-60 ms[32] and in many applications considerably faster switching of pass band wavelength is required to accommodate all wavebands within the available integration time. An quicker alternative is the Bragg Tunable Filter[33] (BTF). A volume Bragg Grating or Volume Phase Hologram (VPH) contains material in which the index of diffraction varies periodically. The orientation of the modulation structure with respect to the incoming light determines whether the grating is reflective or transmissive.

The four designs for snapshot imagers identified as payload candidates for the MA nanosatellite clusters are: waveguide spectrometers[34], Acousto-optic tunable filters (AOTF)[35–37], integral field spectrograph (IFS)[27] and electronically actuated Fabry-Perot Interferometers[38,39]. The designs and trades have been discussed in detail later. Hyperspectral imaging cubes by nanosatellite payloads are also possible using the traditional Sagnac spatial heterodyne interferometers[40]. While this technology have not been discussed in the trade studies, the methods to evaluate and compare it are similar to those used for waveguide spectrometers.

In the recent past, nanosatellites payloads have gone beyond technology and educational demonstrations and attempted to make scientific contributions in Earth spectroscopy. MicroMAS is a hyperspectral microwave radiometer developed by MIT/LL[41] using a high frequency passive radio receiver. VNIR hyperspectrometers for small satellites have been successfully demonstrated in Japan "Taiki"[42] using a Ritchey-Chretien telescope and COTS-obtained CCD image arrays. Aalto-1 is a 400g spectral imager based on a tunable MEMS or piezo-actuated Fabry-Perot Interferometer developed by Aalto University in Finland. Far-IR radiometers based on microbolometers using many options of materials have been developed and tested[43,44]. CanX-2 carries an atmospheric spectrometer, Cloud CubeSat a VIS/NIR camera and a polarimeter and QuakeSat a ULF signal sensor[45]. All these successful small satellite, scientific projects have paved the path for the miniaturization of telescopes as well as visible to infrared detectors using CCD or CMOS arrays, SWIR or FIR thermal detectors, usage of dichroic filters or gratings to disperse the different wavelengths of incident light, on-orbit calibration techniques using infrared lasers/illumination lamps/natural sources. Therefore, while development of HSI for the BRDF nanosatellites seems to be challenging, there are past resources that can help constructively in informing the process.

II. Methodology: Feasibility Evaluation and Baseline Selection Approach

BRDF will be estimated from radiance measurements taken by multiple nanosatellites, each with an identical spectrometer, in two potential architectures: As a formation NFOV cluster sensing the same ground pixel at the same time (Figure 1-left) or as a WFOV constellation with overlapping ground spots (Figure 1-right). The boresight and azimuthal angle of each NFOV satellite sensor with respect to the ground pixel, area of the ground pixel and the required attitude control is calculated from the various proposed cluster geometries, their sizes and altitudes[46].
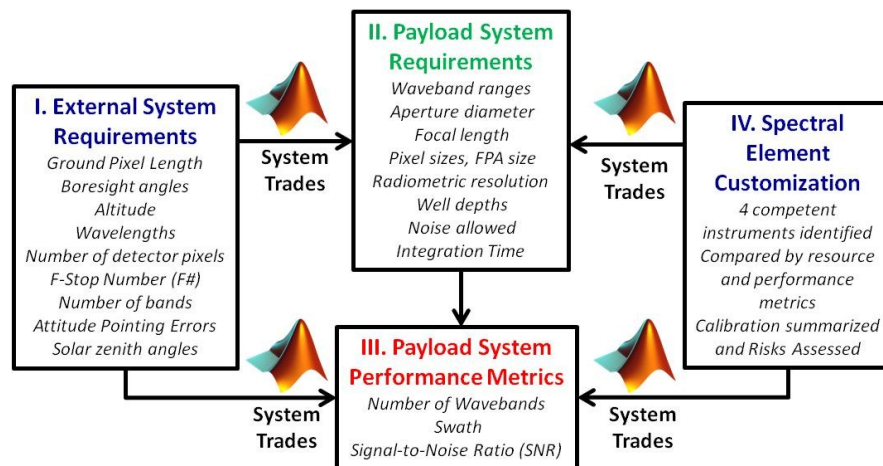

Figure 2: Summary of the modeling approach to design and evaluate hyperspectral snapshot imagers for nanosatellite clusters performing multi-angular earth observation. All simulations have been performed on MATLAB R2013a.

A system tradespace exploration model is used to estimate the dependence of the payload system requirements (Box II in Figure 2) and the system performance metrics (Box III) on external system requirements (Box I) and on the spectral element design (Box IV) as seen in Figure 2. The external system requirements are obtained from either BRDF science requirements derived from heritage airborne missions[5] (e.g. wavelengths, number of bands, ground pixel length), from the cluster geometry model (e.g. altitude, boresight angles) or nanosatellite technology capabilities (e.g. F#, attitude pointing errors). Four spectral element types have been proposed along with a CCD array of Silicone and InGaAs diodes as the detectors for snapshot imaging. They will be compared to each other not only in terms of standalone performance and resources but also on their influence on payload performance metrics. The system trades provide acceptable ranges of payload system requirements which will then be used to design a miniaturized spectrometer that fits inside a nanosat bus. It will be shown that HSI best mitigates the risks of system attitude errors. The performance metrics will provide simple numbers to compare the different payload architectures.

The step-by-step process of the model proposed in Figure 2 to customize an imaging hyperspectrometer as a homogeneous payload for a cluster of nanosatellites that perform multi-angle Earth observation is briefed below. First, the mission level goals are listed – as derived from science requirements and technology constraints. Next, the detailed model connecting the goals to the measurement requirements to the optical system requirements to the system evaluation via functional (technological performance checks) and then form mapping (nanosat bus fitting checks) will be presented. Finally, four unique spectral elements applicable for HSI are identified and customized. Calibration methods for the proposed instruments, both pre-flight and in-flight especially inter-satellite across the DSM, have been listed in the Appendix.

A. Measurement Goals and External System Requirements

The mission measurement goals are derived from the science goals and requirements of current, successful spaceborne instruments and airborne instruments. A spatial resolution of < 500 m is required (from MISR), as are measurement zenith angles up to 60°, measurement azimuth through 360°, solar zenith angles up to 80° (from CAR), spectral resolution varying between 10-40 nm depending on the region of the spectrum, number of wavebands > 14, spectral range between 350 and 2300 nm (from CAR). As mentioned earlier, the exact geometric requirements come from the orbit module of the SE model, driven by spaceborne heritage requirements, and the spectral requirements from the CAR instrument. Since the current instrument being designed is a spectrometer, not a radiometer, the band numbers and widths will be dependent on parameters such as detector types, prevention of spectral aliasing and radiometric range. CAR values will be used as reference (Figure 3). The altitude range considered for spacecrafts is 500 km to 800 km (LEO) because that range corresponds to the most common shared rides available with primary payloads. If all the nanosatellites are launched as the primary payload itself, then the orbit constraints may be removed. The ground pixel length or resolution considered ranges between 100-1000m with an F-Stop number (F#) up to 5.0, which is reasonable for a nanosatellite. The bus requirements are set to mass < 10 kg, physical dimensions < 10X20X30 cm and power < 25W.
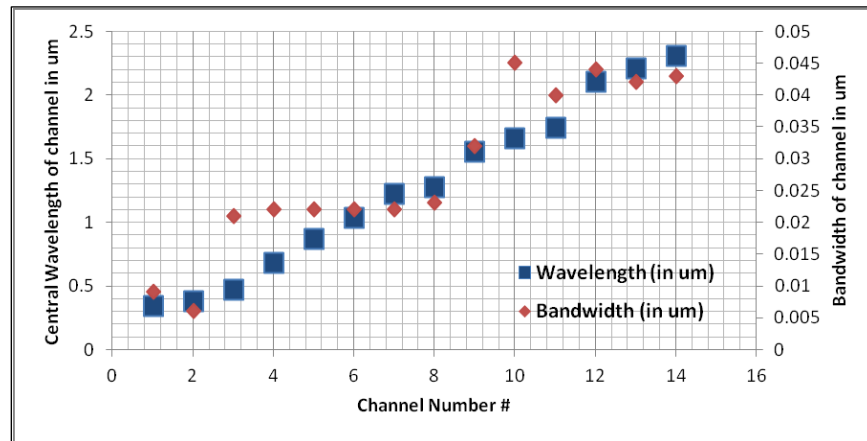

Figure 3: Wavelength requirements for the imaging spectrometer based on the Cloud Absorption Radiometer airborne instrument at NASA GSFC[5]

Measurements will be collected only during daylight because the mission is in the VNIR (near solar) spectrum and the tradespace exploration goal is to maximize swath to increase the overlap of ground spots of all satellites in the cluster and maximize signal to noise ratio (SNR) for improved quality of images.

B. System level Optics Modeling and Payload System Requirements

The high level payload evaluation model has been shown in Figure 4. The design variables are obtained from external requirements and available, appropriate spectral elements (Figure 2). The green variables highlight the simulated optical system requirements and the red parameters the simulated performance metrics to benchmark the different payload system architectures. Each arrow represents a quantitative relationship between connecting variables and parameters as enumerated below. For example, swath is a function of FPA size, slant height, detector pixels # and attitude pointing errors. Interesting trades around the key variables will be described and baseline values chosen after studying the trades.
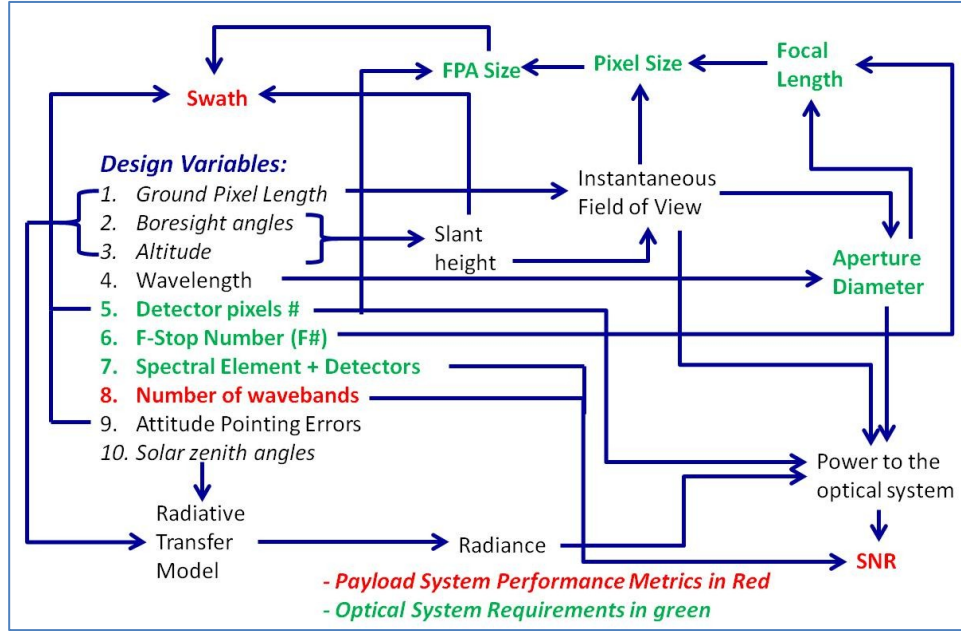

Figure 4: Dependency chart of payload system performance metrics (red, analogous to Figure 2) and optical system parameters (green, analogous to Figure 2) on the design variables, which includes external system requirements, customized spectral elements (also in Figure 2) and the FPA detectors. Each arrow represents an equation which have been enumerated in Section III.

It will be seen later that it is more efficient to divide the spectral range of BRDF interest into sub ranges or bands. Each band is spectroscopically characterized by multiple bins with nearly uniform width corresponding to spectral resolution. The number of bins in a band is given by R:

$$R = \frac{\Delta\lambda}{\delta\lambda} = \frac{BandWavelength\_UpperBound - BandWavelength\_LowerBound}{Bin\_width}$$

Equation 1

Instantaneous field of view (iFOV) depends on the boresight angles (η), altitude (h) and ground pixel size (gps) by Equation 2 through Equation 6[47]. D is the slant distance between the sensor and the ground pixel, λ is the Earth central angle, ε is the elevation angle and ρ is the boresight angle at the horizon – all angular variables are shown in Figure 5. Length of earth's radial vector to the satellite is Re.

$$iFOV(gps, alt, \eta) = \sin^{-1}\left(\frac{gps}{D(alt, \eta)}\right)$$

Equation 2

$$D(alt, \eta) = alt \qquad \eta = 0$$

American Institute of Aeronautics and Astronautics

$$D(alt, \eta) = Re * \frac{\sin(\lambda)}{\sin(\eta)} \qquad \eta \neq 0$$

Equation 3

$$\lambda = 90 - \eta - \varepsilon$$

Equation 4

$$\varepsilon = \cos^{-1}\frac{\sin(\eta)}{\sin(\rho)}$$

Equation 5

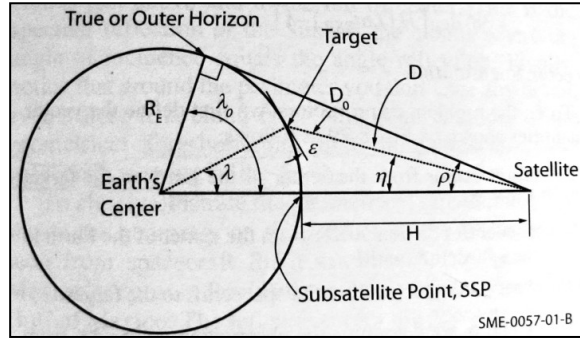$$\rho = \sin^{-1}\frac{Re}{Re + h}$$

Equation 6

Figure 5: Definition of angular relationships between the satellite, target and Earth's center[47]

The pixel size required to capture at least one ground resolution element will be given by Equation 7 and depends on the same variables as iFOV depends on. A pixel size can be selected depending on the altitude, angle and ground resolution needed ($\overline{dp}$ in Equation 8) – for diffraction limited imaging - and the swath achieved by the instrument can then be calculated as a function of its focal length (f) and number of pixels per side of the focal plane array (npix) - Equation 8.

$$dp(gps, alt, \eta) = iFOV(gps, alt, \eta) * f$$

Equation 7

$$swath = \frac{D(alt, \eta)}{f} * npix * \overline{dp}$$

Equation 8

The total power received on the FPA can be calculated by the following equation derived from first principles – conversion of FOV to steradians and multiplying by the angle as well as the aperture surface area:

$$P(\lambda, \eta, h, SZA) = L(\lambda, \eta, SZA) * BW(\lambda) * \left(\pi * Da * \sin\left(\frac{FOV}{2}\right)\right)^2$$

Equation 9

Where FOV = the full field of view achievable using the entire focal plane array as calculated similar to Equation 2, Da = aperture diameter, $BW(\lambda)$ is the width of the spectral bin at λ and $L(\lambda, \eta, SZA)$ (the bin integrated radiance) is obtained from radiation transfer models. This power, multiplied by the optical transmission of the spectrometer, reaches the detectors on the FPA and is integrated over the exposure time. While instrument optical efficiency varies with the spectrometer type, a fixed value of 0.5 has been used in our calculations. Energy received at the aperture is the integration of power received over the exposure or integration time of one image (intTime) - Equation 10. Energy received can be mapped to photon number by Planck's Law (Equation 11) where c = speed of light, λ = wavelength of the image and h = Planck's constant. Integration time available depends on the dwell time of the sensor on any ground pixel (gps) for any given altitude (alt) and on the spectrometer/spectral element type used as will be seen in Equation 15 and Equation 16.

$$E = P(\lambda, \eta, h, SZA) * intTime(totalPixels, nbands, tuningTime, readoutTime, spatialPixels, gps, alt)$$

Equation 10

7

American Institute of Aeronautics and Astronautics

$$S = \frac{E\lambda}{hc}$$

<div align="right">**Equation 11**</div>

The noise components depend on the detectors selected, signal received and stray light. For CCD detectors, it is given by the CCD equation [48] - Equation 12 – where N_* is the total number of signal photons (requirement 9 in the previous section). The major contributors of noise are readout noise (N_R = photons generated when no light shines on the detectors), dark current noise (N_D = photoelectric effect electrons generated by the heat produced by the system or thermal noise that cannot be distinguished from electrons generated by photons) and random sky noise (N_S = photons from background or sky). All the noise factors scale linearly with the number of pixels imaged. Readout noise is assumed to be 5 e$^-$/ (for 16 bit A/D at 1 MBPS readout), dark current 12.5 e$^-$/pixel[49] and detector noise~300 electrons for CCDs[50].

$$\frac{S}{N} = \frac{N_*}{\sqrt{N_* + n_{pix}\left(N_S + N_D + N_R{}^2\right)}}$$

<div align="right">**Equation 12**</div>

Signal to Noise Ratio (SNR or S/N), given by Equation 12, is considered the main determinant of multi-angle image quality in this study. After reviewing past literature on heritage and bigger instruments - SNR of 200 for the airborne AVIRIS instrument [51] and 250 for CHRIS [15] – the SNR requirement is set to a minimum of 100. Practically though, the number of signal photons is lower than the values quoted because they also depend on sensitivity of the CCD detectors which are not able to convert all of the photons that strike the surface into electrons, and so have a lower required SNR. The most important determinants of sensitivity are:

- Quantum efficiency (QE) which is the ratio of incoming photons to those photons actually detected by the CCD and is between 0.5-0.9 in the operational range of the CCD[38]. A constant value of 0.5 was used in our simulations. For AOTFs, the short wavelength response of the camera is limited by the AOTF tuning element and its long wavelength response by loss in quantum efficiency of the CCD camera located at the focal plane.
- System gain which represents the number of electrons which cannot be resolved by the Analog to Digital Converter (ADC)'s bits. More the number of bits available, higher the gain.
- Charge transfer efficiency (CTE) which describes the level of accuracy that the charge stored in each pixel can be transferred from one pixel to another in the readout process and is fixed at 0.8 for SNR calculations.
- Well depth total amount of charge (number of electrons) that can be stored in the pixels before the charge overflows into adjoining pixels through a process called blooming. It is proportionate to the pixel size and a typical value for 3U cubesats is 200 ke$^-$[52] but a limit has not been applied to our simulations.

C. Spectral Element Options and Customization

Heritage spectrometers have traditionally been based on prisms, diffraction gratings, filters, heterodyne-mixers, and interferometers (Fabry-Perot, Fourier transform). Slit based dispersive devices (i.e., prisms, gratings) are best applicable for imaging a vector of spatial elements multi-spectrally. Grating spectrometers employ a push-broom method in time to build a 2D image; the dispersive nature of a grating device limits use in HSI because one dimension is consumed by the dispersed spectrum [53]. Hence the need to adapt other spectrometer designs in HSI. A review of contemporary literature, summarized in Section I-C, revealed four possible HSI designs appropriate for nanosatellites with potential use in earth remote sensing. Their applicability to BRDF specific system requirements is discussed below.

1. Waveguide Spectrometers

In bulk optics, Fourier-transform spectrometer (FTS) devices offer throughput advantages compared to dispersive devices, but they typically involve mechanical modulation of the optical path. Spatial heterodyne spectrometers (SHS) are a static implementation of the classic Michelson interferometer. In one method, the two Michelson mirrors are replaced by diffraction gratings that result in a spatially distributed interferogram. The second method adopts waveguide structures implemented as Mach-Zehnder interferometers (MZI). The waveguide based spectrometers have seen recent popularity due to their compactness and the concept of a "Spectrometer on a Chip." In this instance, multiple waveguide based MZI structures with varying path delays respond to the spectral characteristics of the incident light. Thus, these photonics light-wave circuit (PLC) structures are the basis of the

interference phenomenon that result in the observed interferogram[34]. Advantages of PLC waveguides include miniaturization of spectrometers, exclusion of moving parts, internal vibration suppression, low power requirements, shock resistance and easy radiation-hardening[54,55]. The radiation from a FOV pixel is delivered to an FTS chip. Each pixel from the broad FOV maps to a unique chip in an ensemble. The waveguide spectrometers can be of 2 types:

i. *FTS type based on PLC technologies*. MEMS based FTS systems with a miniature-moving mirror are now commercially available and are an exciting new development. However, these are functionally identical to the traditional Michelson Interferometer. In this section, we focus on the waveguide PLC designs implemented as MZI structures. The incident light illuminates an ensemble of PLC strands. Each strand divides into two arms, and is recombined. The path length difference in the arms is controlled to simulate MZI function in the strand. The MZI structures in the ensemble have varying path differences to simulate phase delay in a mechanically modulated Michelson interferometer (Figure 6 – left panel). The recombined beams in each MZI results in interfere at the detector commensurate with the path difference. Thus, the spatially organized MZI structures and detectors measure an interferogram which forms a Fourier transform pair with the original spectrum. The spectral information is encoded in the interferogram samples, and a Fourier transform returns the original spectrum [56].

Equation 13 shows that the relationship between the input and output power of a waveguide FTS in the limit of a discrete cosine transform [56], where $\bar{\sigma} = \sigma - \sigma_{min}$ is the modified wave number, σ the wavenumber, σ_{min} the minimum detected wavenumber, N the number of waveguide strands, Δx the maximum optical path delay desired (function of propagation efficiency and waveguide length) and x_i is the effective optical path length delay. Calibration errors can also be calculated from the inverse relation of Equation 8 using linear regression applied to inteferogram points for a matrix of path delays.

$$p^{in}(\bar{\sigma}) = \frac{\Delta x}{N} p^{in} + 2\frac{\Delta x}{N} \sum_{i=1}^{N} W(x_i)F(x_i) \cos 2\pi\bar{\sigma}\, x_i$$
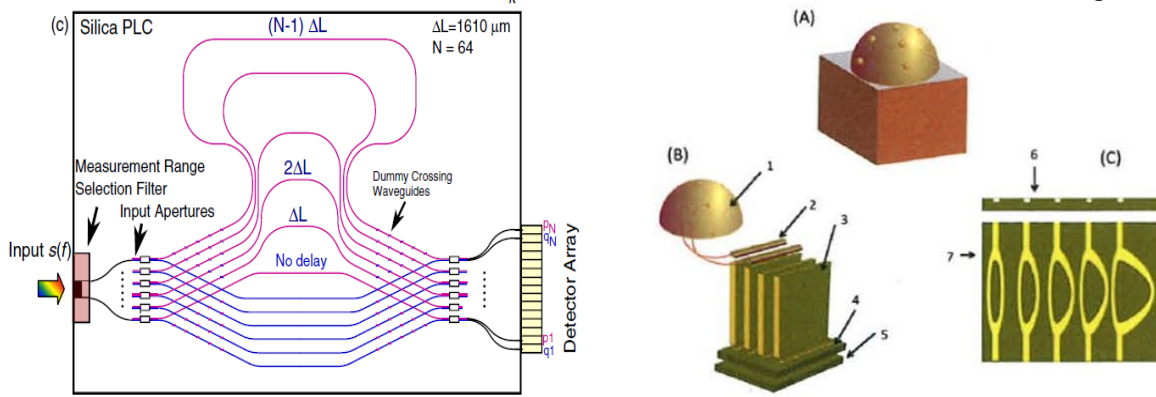
Equation 13

Figure 6: The left panel shows the paths inside a Fourier-transform, integrated optic spatial heterodyne spectrometer on a Si-based waveguide[55]. Light enters the waveguides on the left and produces an interferogram on the detector array on the right. Fourier transform of the interferogram gives the original spectral distribution. The right panel shows the schematic view of the Addressable Photonics Cube (APC) within the Spectrometer on a Chip in (A) and its components in (B)[54]. The components include a dome with apertures to let light in from different directions(1), fiber-optic couplers(2), Spectrometer on a Chip modules (3), 2D detector array (4), FPGA (5). (C) shows the Spectrometer on a Chip components – the waveguides.

ii. *Grating type based on PLC arrayed* . In traditional grating devices, the focal plane field is the result of multi-beam interference of the diffracted beams. Implementation of the dispersion principle using waveguide involves Fresnel [57] or Fraunhofer [58] limits for diffraction fringes and form the class of AWG devices. In conventional grating spectrometers, wavelength resolution can be improved by reducing the slit width leading to a reduction in optical throughput. The interference approach using waveguides decouples the relation between input slit and resolution and thus allows more throughput per resolution bin than traditional gratings [59]. The design for a SHS device using two interleaved AWG devices is in recent literature[58]. Monochromatic light produces sinusoidal

fringes of period dλ while an arbitrary input spectral density B(λ) will produce an interference pattern I(x) where x is the position along the interference pattern as given in Equation 14.

$$I(x) = \int_0^\infty B(\lambda) \left[1 + \cos \frac{2\pi}{d(\lambda)} x \right] d\lambda$$

<div align="right">**Equation 14**</div>

The interleaved arrays produce two wave fronts that propagate and mutually interfere in the slab waveguide yielding wavelength-dependent fringes. This is due to the different dispersion of the arrays which makes the wave fronts intersect at different angles for different wavelengths thus forming wavelength-dependent fringe patterns as shown in Figure 6-left. In general the input spectrum is related to the fringe pattern via Fourier transform since any input signal can be decomposed into its monochromatic constituents. This interleaved AWG arrangement allows using a wider input waveguide width compared to a standard AWG of similar spectral performance.

The FTS type has important advantages over the grating type – they have large optical throughput for the same spectral resolution because of the lower probability and intensity of 'crosstalk' between the different waveguides [60], ability to calibrate theoretically for ideal path delay and through simulations for non-ideal delay [56] and ability to correct interferometric defects in the post processing phase [55]. The main performance criteria are spectral range and resolution, optical crosstalk, optical loss and polarization wavelength dependence. Visible and near-infrared devices have been reported by researchers[59,60]. NASA GSFC is currently developing the mid-infrared waveguide FTS for multi-angular radiance measurements (Figure 6, right) and is expected to have a compact design.

If the length differences of the waveguides vary linearly from 0 to L_{max}, the number of waveguides needed is given by Equation 15 where $\Delta\lambda$ is the spectral range of the spectrometer, $\delta\lambda$ is the spectral resolution and R is the number of wavelength bin elements as defined in Equation 1. For a FTS type device, L_{max} is a function of resolution, central wave number and efficiency, the number of waveguides needed[59] (Equation 16).

$$N = 2 \frac{\Delta\lambda}{\delta\lambda} = 2R$$

<div align="right">**Equation 15**</div>

$$L_{max} = \frac{R}{k_0} \frac{2\pi}{n_{eff}}$$

<div align="right">**Equation 16**</div>

While FT spectrometers without moving parts (also in the SHS class) have been developed and flight-tested for UV (SHIMMER [59] launched in 2007) and IR wavelengths (SHOW [60] not launched yet), the development of the equivalent on PLC technologies is less than 5 years old. Its TRL is estimated to be between 5 and 6. One of the biggest constraints in the development cycle is to develop methods to eliminate crosstalk between adjacent waveguides which is estimated to increase with decreasing bandwidth [57].

2. Acousto-Optic Tunable Filter Spectrometers

Acousto-optic tunable filters (AOTF) offer a mechanism to filter broadband incident light by achieving the spectral decomposition in time due to its high spectral agility, and therefore allows HSI. An AOTF device[35–37] can switch from one spectral range to another in the time that it takes an acoustic wave to traverse a solid state crystal (typically tens of microseconds). An acousto-optic cell – marked in the top panel to the left of the CCD detector in Figure 7- is a transparent birefringent crystal excited by a radio frequency transducer. Acoustic waves propagate inside the crystal and create regular spatial variations of the refractive index. Under phase-matching conditions, light of a particular linear polarization and wavelength, incident on the crystal at a very specific angle, is diffracted by the moving grating produced by the acoustic wave. The conditions favoring diffraction are only satisfied for a particular spectral frequency at a particular incident angle and a particular driving frequency so by controlling the transducer frequency, the spectral frequency diffracted can be selected. Controlling the transducer power allows control of the amount of light diffracted. Typical transducer power is on the order of 3-4 W[35–37,63]. While higher transducer power increases the amount of diffracted light, it also degrades spectral resolution by increasing side lobes of the center frequency. Although a number of birefringent materials have been used for AOTF devices, TeO_2 is a frequent choice

due to its high acousto-optic figure of merit, and good transmission in the visible and infrared, (350 nm -5000 mm). Other materials include TAS, which is transparent to 11 μm, and quartz which is transparent in the UV.

AOTFs can be used for HSI because the AOTF can be tuned to the first desired band, the 2D spatial matrix imaged at that band, signal response over the integration time period, CCD read out and the process repeated for the next wavelength band until all wavebands are exhausted. While this restricts the integration times as will be seen in trades presented in the next section, AOTFs offer the advantage that only two spectral elements are needed for the entire spectral range because the ranges will only depend on the detectors used at the end of the AOTF cell – Silicon or InGaAs. This is in contrast to waveguides where the range has to be divided into 4 wavebands to also account for the free spectral range. The AOTF spectrometer has two units – Optical which consists of fore optics, AOTF crystal, imaging optics and the camera as seen in Figure 7. The Electronic unit controls the AOTF, Camera, power supply, etc. The weight of the optical unit is in the ballpark of 1 – 1.2kg, the electronics within 0.5 kg to 0.7 kg which brings the total spectrometer mass to within 4-5 kg [32]. AOTFs have significant heritage since they were used recently on the Mars Express [64], the Venus Express [65] and also to probe Titan's atmosphere back in 1999[63]. The TRL of this spectrometer design can thus be estimated at 8-9.
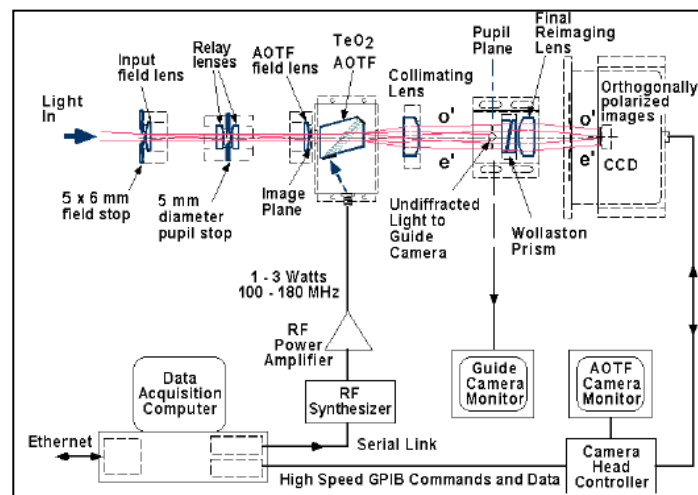

Figure 7: Detailed AOTF system as published in [37]. It shows the AOTF cell in the center and its interfaces with the front end optics and back end avionics [66]

3. *Integral Field Spectrograph*

An integral field spectrograph (IFS) is a 3-D-type device that can gather spectra at every spatial element in its field of view. Although IFS-type instruments are used primarily in ground-based observatories, including the Keck Observatory in Hawaii, the technology has been demonstrated in spaceflight through the TIGER program using lenslets [27] and through the ARGUS program using optical fibers which connected the hexagonal aperture to a single vector imager [31]. IFS using lenslets is currently being used in the development of the CHARIS instrument to look for exoplanets on small satellites, thus is the chosen approach of the two.

An IFS simultaneously obtains spatial and spectral information over the field of view by dispersing the entire image on the detector using lenslets to sample the image plane [67]. Each lenslet samples a piece of the image and focuses it to a point spread function (PSF). Each PSF is dispersed and then imaged by the multiple detector elements as seen in Figure 8. This allows the IFS to measure two spatial and one spectral dimension simultaneously by mapping all 3 dimensions onto the 2D detector plane by spreading the spectrum over multiple spatial pixels. IFS offers the advantage of low mass and volume as well as a medium TRL (5-6) for the technology and low TRL (3-4) for the same in small satellites, especially for non-astrophysical observations. The disadvantage is that each dispersed spectrum for a spatial pixel may take up to 35 detector pixels in length and 6 pixels in width (focused by a lenslet element)[67] causing a significant reduction in the number of pixels available for spatial imaging. Additional beam resizing will be needed to focus the image on the larger pixel than that required from the trade-space analysis

in Section III, hence more volume. Finally, processing required to deconvolve the spectral and spatial data from the same detector array may be complicated.
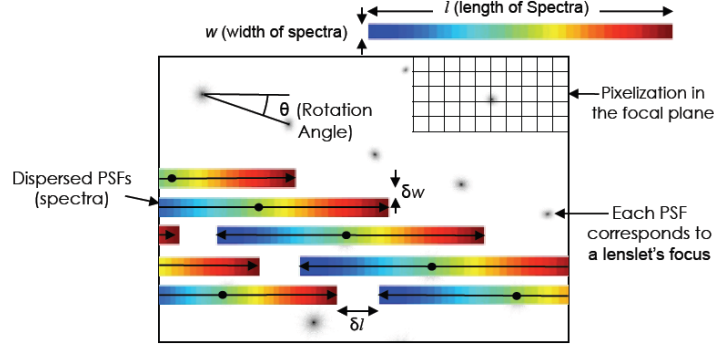

Figure 8: The layout of the spectra and pre-dispersed PSFs on the detector of an IFS as published for the CHARIS instrument [67]

4. *Electronically Actuated Fabry Perot Inteferometers*

The traditional Fabry-Perot Interferometer[32] (FPI) has been used as a tunable filter since its invention. In the concept of using an FPI as a hyperspectral imager, light from the object is collimated by the front optics and the collimated beam is directed to the FPI cavity and order sorting filter. This combination passes only one narrow wavelength band determined by the air gap value and the selected FPI order filter. The focusing optics focuses the light transmitted through the FPI to an object image at one narrow wavelength band. It obvious that the light beam through the FPI is not totally collimated and that this will have an effect on the spectral resolution of the instrument. When low orders of the FPI (1 - 4) are used the spectral resolution is not dominated by the collimation level of the optical beam as far as the incident angle is below around 5 degrees.

The air gap value of the FPI and hence the order of FPI can be scanned from 0 to tens of micrometers by Piezo actuators and the images are recorded as a function of air gap width[68]. For each pixel, there is a signal as function of the air gap value containing the information of the spectrum of the light entering the FPI. The spectra of the studied light can be retrieved from the measured signal using a dedicated Fourier transform based algorithm. This concept has been used for the development of the primary payload of the Aalto-1 cubesat developed by the Technical Research Centre of Finland[38,39]. They measure the RGB image data at the air gap value range and intervals derived from the spectral range and sampling requirements. For a selected air gap value the signals of the B-, G- and R-pixels are given by the theoretical spectral responses or transmittances integrated over the waveband. COTS multispectral sensors for the UV and VNIR ranges can easily be obtained from Ocean Optics Inc. and Silios Technologies. The total operating range is 400 – 1100 nm and spectral sampling below 1 nm is possible for a stability of 0.1 nm. Time required to change the wavelength band is less than 2 ms, F# < 4.0 is supported along with a full FOV up to 20°. The entire instrument fits within a 110 mm X 75 mm X 55 mm envelope, weighs less than 350 g and consumes an average of 3W. Cubesat compatibility will be demonstrated on orbit because the instrument is due to fly on the Aalto-1 satellite to be launched in late 2013.
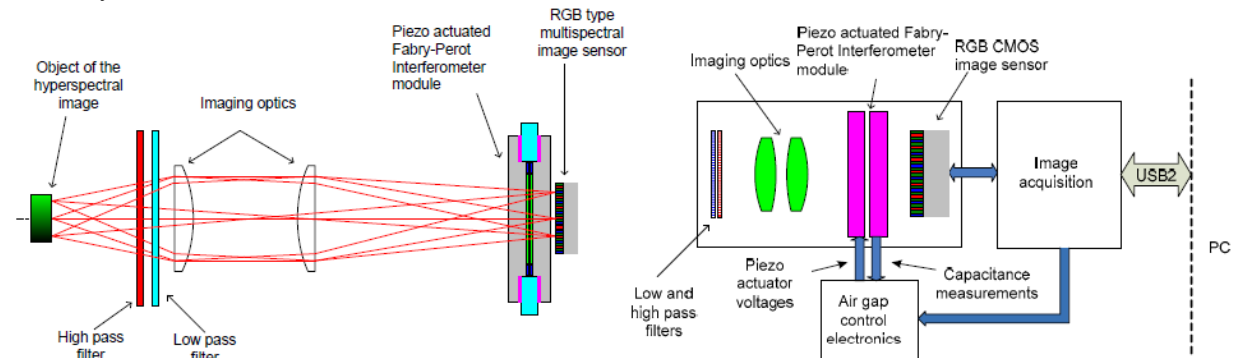

Figure 9: Fabry-Perot Interferometer and multispectral image sensor based hyperspectral imager optical concept and block diagram of a control and data acquisition electronics as published in Saari et. al.[38]

III. Modeling Results

This section presents results of the model processes proposed in the previous section. First, the mapping from measurement requirements to the optical system requirements to the system evaluation is presented. The different spectral elements are evaluated relative to each other. Finally, all the mission parameters – constants, constraints and variables – will be traded to identify some baseline architectures for the hyperspectral instrument within acceptable ranges of the performance metrics.

A. Radiative Transfer Modeling

Signal to noise ratio (SNR) is one of the most important metrics for determining the performance of the optical system. It is calculated by integrating the radiance at a given altitude over the area of the aperture and integrative time (dependent on the ground velocity). Radiance can be estimated using an atmospheric radiative transfer model e.g., SBDART from the UCSB (Santa Barbara DISTORT Atmospheric Radiative Transfer Model) or COART (Coupled Ocean-Atmosphere Radiative Transfer) from NASA Langley or available datasets from existing missions, examples being MODIS, MISR, POLDER. The Coupled Ocean Atmosphere Radiative Transfer (COART) model [69], a publicly distributed software for radiative transfer by NASA, was used to calculate the radiance in $W/m^2/sr/\mu m$ at an altitude of 100 km (the highest available) for different solar zenith angles (SZA), sensor boresight angle (η) and wavelength of radiation (λ). This radiance can be integrated over the aperture area, wavelength binwidth and solid angle of the field of view (FOV) to calculate the power received by the optical system. SNR is a function of this received power and is dependent on the spectrometer type.

Figure 10 shows the COART model radiances as log10 for SZA = 0°, 40°, 80°. The maximum and monotonically increasing variation is seen for the visible (400-700 nm) and NIR (700-1400 nm). There is a drop in radiance in the UV and SWIR regions. Increasing SZA angles leads to more outward radiance because the earth radiates more during sunset than noon. The boresight angle dependence is very little compared to dependence on wavelength and SZA, however, it becomes more important with higher SZA. It is important to note, though, that the COART model has been developed to match available sensor data and since hardly any missions have successfully sampled the boresight angular variation of radiance therefore the variation with respect to angles may be underrepresented in these charts. The numbers are intended only for nominal calculations of expected SNR to design the payload. Since there is nothing significant to affect the radiation transfer above 100 km, the radiance measured at 100km can be assumed to be the same at LEO altitudes[9]. The COART model results show the range of variation of radiance dependent on the time of the day as well as the atmospheric transmission windows. This knowledge helped determine the wavelength band limits in the spectrometer so that the measurements are within the radiometric range of the detectors for those bands.
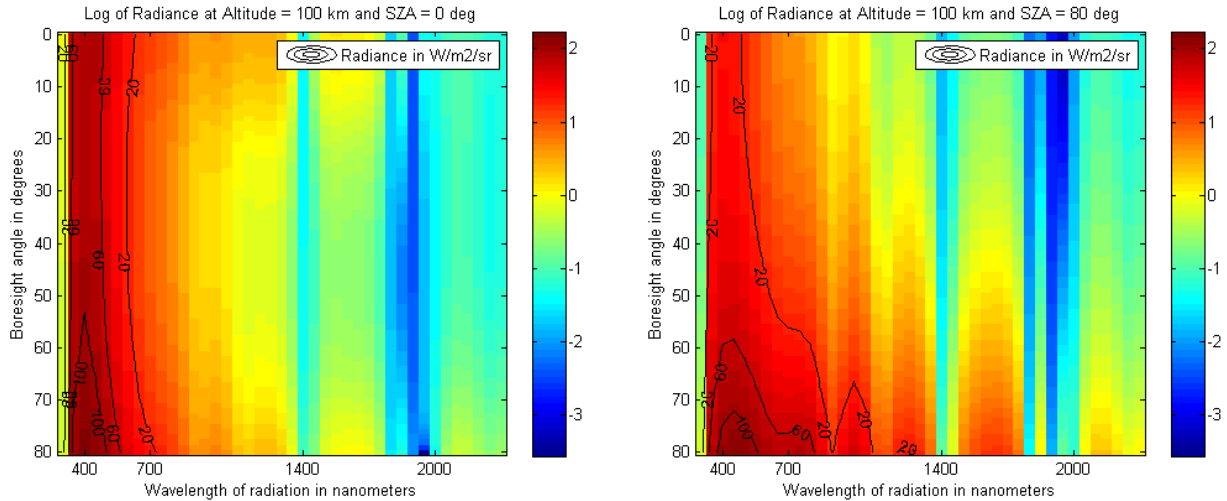

Figure 10: Radiance at 100 km altitude as provided by the COART model for atmospheric radiative transfer for varying sensor boresight angles and radiation wavelength, for solar zenith angles of 0° and 80° as a heat map

---

[9] Confirmed via an email conversation with Dr. Zhonghai Jin, the primary programmer of the COART model

B. Functional Mapping of System Goals to System Requirements

The relationships in Figure 4 and Equation 2 through Equation 12 can be used to map some of the measurement goals to optical system requirements (green) and metrics (red).

Selection of the wavelength bands for the spectrometer depends on the following criteria: Free spectral range of the central wavelength (spacing in optical wavelength between two successive reflected intensity maxima) to prevent spectral aliasing, spectral range of detectors available and radiometric range of detectors available. To prevent the overlap of one dispersive order of a wavelength with the lower order of a higher wavelength, no band can contain an integral multiple of a wavelength it contains [53]. Silicon detectors work best between 350 nm to 1000 nm while InGa, InAr or GaAs detectors work best for the NIR to short wave IR range of 1000 nm – 2500 nm [70]. InGaAs is picked as the detector of choice because it has high D* (detectivity), low dark current, and responds to the whole SWIR range for modest cooling (150K-200K as demonstrated in ESA's SCIAMACHY instrument [71]) so that a major portion of the instrument's mass and power budget is not consumed by the focal plane cooler. Finally, the power received by any detector should not vary by more than the square root of its order – this is based on the assumption that the random noise in the detector can at most be the square root of its maximum signal which can at most be the detector's well capacity.

Table 1: Potential wavelength bands and corresponding bins for the proposed spectrometer

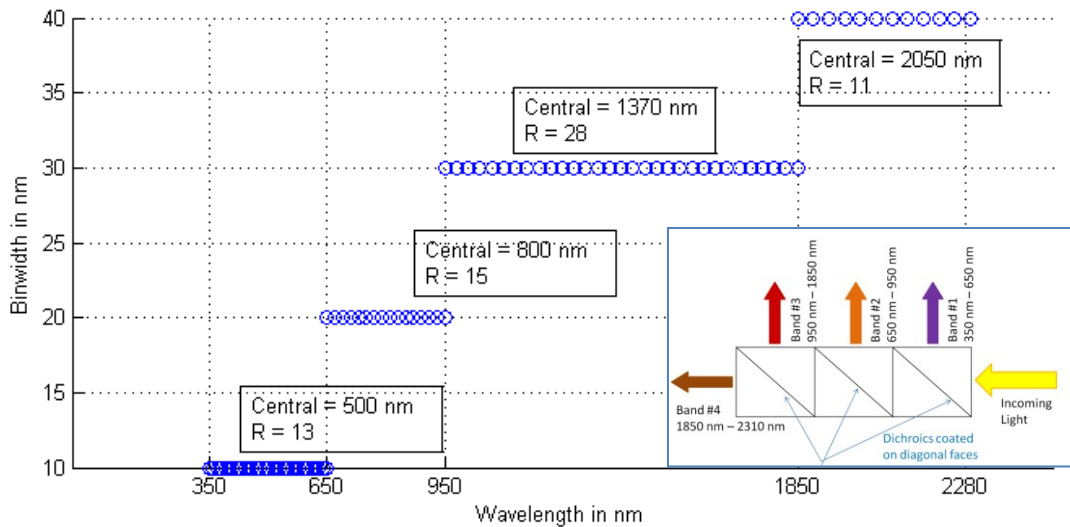| Band #	Wavelength lower bound (nm)	Wavelength upper bound (nm)	Central Wavelength (nm)	Binwidth (nm)	Number of Bins
1	350	650	500	10	30
2	650	950	800	20	15
3	950	1850	1370	30	28
4	1850	2310	2050	40	13

Figure 11: Proposed wavelength bands for the spectrometer, their corresponding bins and binwidths. The boxes show the central wavelength and resolution (R = Δλ/δλ) for the 4 bands. The inset shows the proposed design for producing 4 wavelength bands for input into 4 spectral elements, achievable in a small volume of [1" x 0.5" x 0.5"]

Optimizing all the requirements gave the following band distribution – listed in Table 1 and shown schematically in Figure 11. Four wavelength bands are proposed, that is, the incoming light would need to be split into these four bands using dichroics as shown in Figure 11's inset, such that the bounds and central wavelength correspond to Table 1 and binwidth of the bins within the individual bands monotonically increases with wavelength. Figure 11 thus shows that longer wavelengths have more spread out spectral bins. Binwidths have been chosen with reference to the CAR instrument (Figure 3) and to compensate for the drop in radiance energy with increasing wavelength and

thus operate within acceptable radiometric range. The number of bins (R) to be imaged can be calculated from Equation 1 where the variables correspond to Table 1.

IFOV required for a given gps clearly decreases with increasing altitude and this is more pronounced at larger nadir angles due to large increases in the slant distance with increasing altitude. IFOV required for a given nadir angle increases by relaxing the resolution requirement (gps), more so for vertical viewing than tangential. Given the wavelength of radiation and iFOV, the diffraction limited aperture diameter can be calculated. For an F# of 1.5 (derived from heritage instruments with BRDF products) focal length and then, for one detector pixel per ground resolution element, the required pixel size can be calculated. For a selected and constant aperture diameter, the diffraction limited spot size for lower wavelengths will be much smaller than higher ones. Therefore, the diffraction limited pixel size calculated from near-IR will limit the resolution available to UV wavelengths 'for the same aperture diameter. For different wavelength bands, it is possible to calculate the pixel size from the F# for finer sampling of those bands. The F# has also been varied to show its dependence on the focal length and pixel-size later. The number of detector pixels requirement constrains the swath and the focal plane array size.
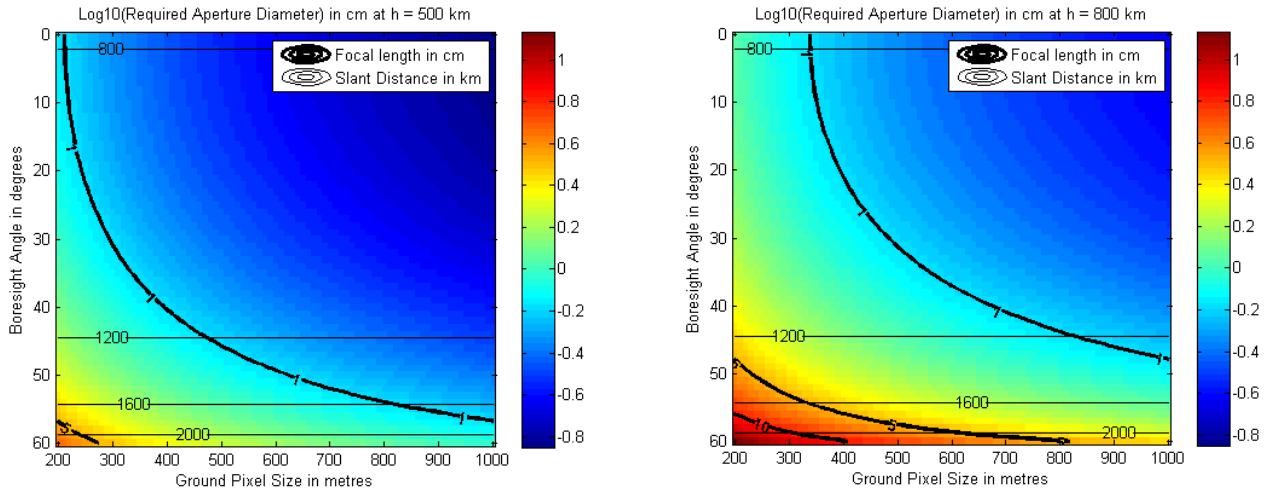

Figure 12: Variation of required aperture diameter (as log10) at altitudes = 500km, and 800 km over boresight angle to the ground pixel and ground resolution. The corresponding required focal length and the slant distances for the boresight angles are contoured. The best design is on the bottom left corner of the right panel.
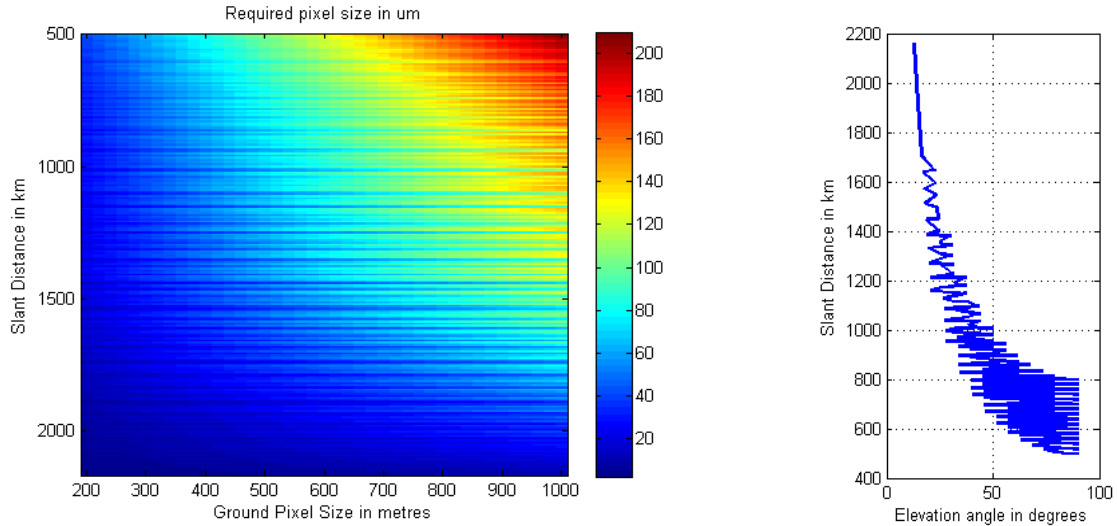

Figure 13: Required pixel size on the Focal Plane Array (FPA) as a function of slant distance (function of altitude, boresight angle and elevation) and ground resolution. The oscillatory characteristic is due to the dependence on elevation. The best design is on the bottom right corner of the left panel.

Assuming the highest wavelength to be 2300 nm, Figure 12 shows the variation of the required aperture diameter (plotted as log10 to exaggerate the variation for larger ground pixels) and focal length (contoured in bold black) for diffraction limited imaging at altitudes of 500 km and 800 km. Slant distances to the ground pixel (D) have been contoured in plain black. The highest focal lengths and diameters are needed for highest angles, slant distances and resolutions (tightest iFOV requirements) which are the Pareto utopia points. Thus for Pareto optimal performance at 350 m spatial resolution (NFOV), the diameter can be baselined at $10^{0.7} = 7$ cm and the focal length = 10.5 cm for a constant F# of 1.5 – which are all feasible within nanosatellite or 6U cubesat size constraints. The diameter can be increased if the energy simulated through this aperture and thus SNR do not meet the measurement requirements. If higher F# are technologically achievable, then the optics sizes may be further reduced and greater spatial resolution may be achieved. For WFOV payloads, the spatial resolution constraints should be much higher to allow for much larger ground footprints therefore the required aperture diameter can be smaller for diffraction limited imaging.

Assuming the baseline diameter of 7 cm, focal length of 10.5 cm and one pixel on the FPA per ground resolution element, the required pixel size can be calculated as a function of boresight angle, altitude and ground resolution. Combining the first 2 variables into one, Figure 13 – left panel - shows the required pixel size as a function of slant distance (function of altitude, boresight angle and elevation) and ground resolution. The right panel shows the dependency of slant distance on elevation angle therefore causing the oscillatory characteristic of the graph with sharp transitions. Figure 13 shows that the smallest pixels are needed for highest angles, slant distances and resolutions (tightest iFOV requirements) which are the Pareto utopia points. Thus for Pareto optimal performance, the pixel size can be baselined at 20 μm for one pixel per ground pixel for diffraction limited imaging at 2300 nm. Since the diffraction limited spot size decreases with wavelength, as given by Equation 17, more resolution is achievable (for the same aperture diameter of 7 cm) on the FPA than 20 μm if the pixel size is made smaller fo smaller wavelengths. Equation 17 is a product of diffraction limited iFOV and focal length.

$$dp = 1.22 * \lambda * F\#$$

<div align="right">**Equation 17**</div>

The pixel sizes required to operate at the respective diffraction limits of the central wavelengths of the four potential instrument bands (500 nm, 800 nm, 1370 nm, 2050 nm) are calculated from Equation 17 and relaxed to be 1 μm, 1.5 μm, 3 μm and 4 μm. Thus, while 20 μm is the maximum pixel size that will fit the Rayleigh resolution criteria for the longest wavelengths, 1 μm, 1.5 μm, 3 μm and 4 μm are the minimum pixel sizes for pixel delimited imaging. Since pixel limited imaging comes at the cost of swath size, which is already very narrow, it is not preferred for extended object earth observation. For WFOV payloads, large swath and thus large pixel sizes are required (Equation 8). This would imply far lower ground resolutions than NFOV (Equation 7) payloads, smaller required optics for diffraction limited imaging and lower possibilities of pixel delimited imaging.
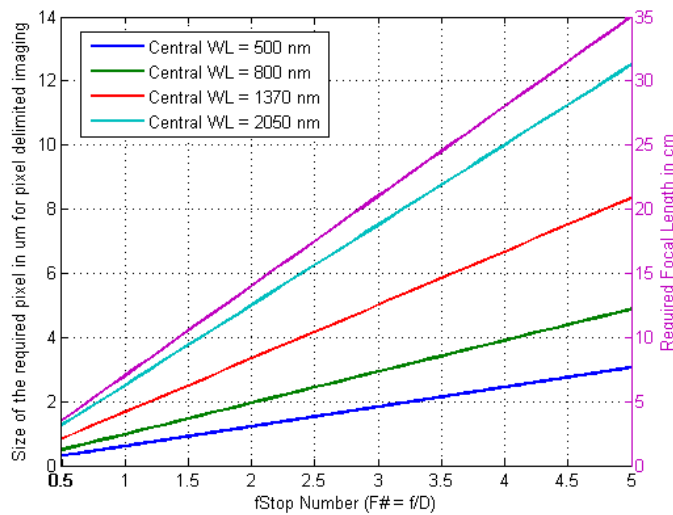

Figure 14: Dependence of pixel size required to achieve pixel-delimited resolution and focal length on F# for an aperture diameter of 7 cm.

Figure 14 shows that varying the F# number or the lens speed of the camera changes the required focal length of the system (marked in magenta) and the required pixel size to resolve up to the diffraction limit of every wavelength range/band (marked in all other colors). An F# of 1.5, as assumed in the previous trades, needs a focal length of 10.5 cm which is achievable in 6U cubesats but if a further focal length reduction is required, the aperture needs to be smaller than 7 cm or a larger F# needed. Aside of engineering complexity, the trade-off is that the detector pixel sizes need to be even tighter to maintain the same resolution.

C. Spectral Element Modeling

For waveguide spectrometers, given the spectral ranges in Figure 11 and Equation 15, the total number of waveguides needed will be 2 * 85 = 170 – which has been demonstrated in the laboratory and published in literature [57,58]. For a 6 μm pitch of the waveguides [57], the chip breadth will be ~12 mm (6 μm pitch times 200 waveguides). The length of the chip needed would be given by L_{max} in Equation 16[57] where R is the resolution, k_0 is the wavenumber and n_{eff} is the mode effective index. For the wavelength resolutions and central wavelengths proposed in our spectrometer's 4 band ranges, the corresponding L_{max} for the ranges are 18.75 mm, 15 mm, 47.95 mm and 33.3 mm. Thus, the length of the chip for the 4 wavelength ranges should be at least L_{max}. The thickness of the chip is the length of a waveguide and the glass required to etch it (cradle size), less than a 1 mm. Each chip is therefore estimated to be ~ 12 mm X [18.75 mm, 15 mm, 47.95 mm, 33.3 mm] X 1 mm. For 1600 spatial pixels, 1600 chips will be needed which will occupy a volume of less than10 cubic cm or the size of one cube in a Cubesat. This compact volume is possible because the Mach Zehnder waveguide strands can be interleaved to reduce the collective volume by 2-3 times compared to the simple stacked layout [58]. Technical challengers involved in fabricating such path differences may be relaxed with the use of high refractive index materials as substrates; thus, we assumptions represent upper limits for the length dimensions. If a separate dispersive unit is needed for each wavelength band, then 4 such cubes will be required, causing this design to be a pretty large by nanosatellite standards. The electronics associated with the operations weigh less that 0.7 kg and the chips are less than a milligram, easily achievable within nanosatellite mass constraints. This design can be used for HSI because each spatial pixel has its own chip, thus the arrangement of the pixels as a vector or matrix is not important.

For Integral Field Spectrographs, a spatial range of 1000X1000 pixels (a typical nanosatellite imaging baseline) will require 35000X6000 = 210 million pixels! Conversely, holding 1000X1000 pixels constant implies that we would have to settle for 35 times less FOV than the other spectrometer designs can provide. While, at the CHARIS available detector pitch of 18 μm, the volume is not much (2.5 cm X 0.4 cm), the cost scales up tremendously because of the spatial scale we wish to achieve. The modeling of AOTFs and FPIs will be discussed in detail in Section III-D because both image the spectrum temporally and hence affect both SNR and swath size.

The spectral element designs identified in Section 2 are now summarized in Table 2 in terms of their relative fit within nanosatellite resource constraints and the relative performance with respect to standard spectrometer parameters. All four can fit within the mass, volume and power requirements of small satellites, as enumerated in the previous section. Since they are low compared to traditional designs – the table shows their relative rank among each other.

The spectral element performance metrics to compare waveguide spectrometers to the three other designs introduced in Section II-C are:-
- *Required number of pixels to achieve the same spatial and spectral coverage and resolution*: IFS samples 3D onto a 2D array thus needs an order of magnitude more pixels. AOTFs and FPIs sample the spectral dimension in time and therefore do away with the requirement of more pixels and varied spectral elements to account for bands (with different bins)
- *Susceptibility to spatial and spectral aberrations:* Waveguide FTS and FT-FPI spectrometers rely on the Fourier transform of the spectrum, aberrations can be compensated for mathematically [54]. FT-FPI has the additional advantage of time domain imaging. IFS runs the risk of overlap of the spatial and spectral components if the lenslet focuses erroneously hence leads to higher aberrations if not deconvolved correctly.
- *Achievable resolution for the same aperture diameter:* AOTFs have been demonstrated in space with a field stop of 1-2 cm for the AO cell however the cell can be connected to a large aperture telescope (>2 m used for imaging Titan [63]) however, the more the ratio of apertures, the more the required focusing optics or beam

resizing required to maintain the resolution. The first tunable FPI on a cubesat is yet to be launched, therefore has a significantly lower TRL than AOTFs. The CHARIS design (IFS) can operate at three different observation modes of varying spectral resolution of R = 14, 33, and 65, which are all relatively lower than AOTFs and much lower than waveguides are capable of at the same slit size.

- *Optical throughput of the full system:* It is very high for waveguide spectrometers with well prevented crosstalk, even compared to large traditional spectrometers, because they use total internal reflection with minimal loss of energy between the filters and the FPA
- *Possibility of measuring the Stokes' vector or polarization state from the incident light*: Since AOTFs use the birefringent crystals, the index of refraction of the "ordinary" axis differs from that of the "extraordinary" axis. By imaging 2 diffraction orders (-1 and +1), it is possible to calculate polarization with some addition to system size. IFS also has the possibility to expand to include polarization [72] capabilities but for a much higher addition of pixel numbers than waveguides. FPIs have not demonstrated polarization capabilities yet.
- *Possible spectral range within the UVNIR spectrum:* AOTF crystals are made of TeO_2 which, for practical applications, is transparent above 350 nm. The CAR airborne instrument has a band of interest at 330 nm which cannot be sampled using AOTFs unless a bandpass filter is applied for the UV range and quartz is used as the crystal, which in turn requires more transducer power. FPIs in Aalto-1 have a maximum range of up to 1100nm. Waveguides have much more flexibility in spectral range as do IFS, but for a much higher number of pixels.

Table 2: Comparison of the selected spectral elements in terms of resource and performance metrics. The colors indicate whether the parameter evaluation is good (green), acceptable (yellow) or bad (red) compared to the other three instruments considered.

Spectrometer Types in terms of Spetcral Elements:	Waveguide Spectrometers [60]	Acousto-Optic Tuning Filters [36]	Integral Field Spectrographs [67]	Tunable Fabry-Perot Inteferometers [38]
Spectral Element Resource Metrics:				
Mass	Medium	Low	High	Low
Volume	High	Medium	Medium	Medium
Power	Low	High	Low	High
TRL	Low	High	Low	Medium
Spectral Element Performance Metrics:				
Required Num of pixels	Medium	Low	High	Low
Susceptible to aberrations	Medium	Low	High	Low
Resolution per aperture	High	Medium	Low	Medium
Optical Throughput	High	Medium	High	Medium
Polarization Measurement	Medium	High	Low	Low
Spectral Range	High	Low	Medium	Medium

One specific design out of the above three is hard to select from the parametric study since the metrics evaluated in Table 2 cannot be compared to each other using numerical weights (apples to oranges problem). Assuming equal weight and a score of [1, 0.5, 0] for every [green, yellow, red] box, normalized averages show that AOTFs emerge at the top with a 65% score followed by waveguides at 60% , FPIs at 55% and IFS at 30%. Waveguide spectrometers, given 2-3 years of development time and subsequent increase in their TRL, will catch up with AOTFs as an equal candidate. FPIs need more than a year to raise their TRL to 6 (depending on Aalto-1's success), however will still be below AOTF's consistent success in flight heritage. Both AOTFs and FPIs they need active power for tuning the spectrometer and are spectrally constrained without increasing power further. Given the current status, AOTFs are concluded to be qualitatively appropriate for the mission. The next section will compare the top three designs quantitatively and show that other designs outperform AOTFs in expected performance.

D. Payload System Performance Metrics

   This section discusses the payload system performance metrics – swath and signal to noise rations (SNR) – as they vary with the selected design variables and calculated optical system parameters for NFOV payloads.

   The number of pixels on the square FPA is considered to be at a maximum of 2000 pixels per side. Previous nanosatellite missions have used from 1024 to 2048 pixels per side[38] and COTS FPAs of up to 1260 X 1260 pixels with InGaAs detectors with spectral range up to wavelengths of 2.6 μm have been documented in literature [73], which makes the value COTS achievable. The baseline case will be 1000X1000 pixels to simulate the most stringent requirements, unless other requirements push the number down further. This corresponds to an FPA side of 1 cm, which is achievable within nanosatellite optics (as is 2 cm for 2000 pixels).

   It is important to note that the true swath for a cluster of satellites imaging a common ground target is actually the overlap of individual swaths of the satellites. Therefore, the true swath is a percentage of the individual swaths, dependent on the attitude control errors of the satellites – as shown in Figure 4. The swath is wavelength independent and ground resolution independent because a constant pixel size suited for diffraction limited imaging (20 μm) was assumed.

   Whiskbroom scanners have not been considered for mission trades because they have mechanisms that increase the risk of failure and have rotating elements that may disturb the attitude control system, which is critical for correct payload pointing. For push broom sensors, the "swath" in the along track direction is only one ground pixel (gps) wide. Thus, for a mission that requires images that capture simultaneous angular data, push broom scanners have the disadvantage of being extremely susceptible to attitude control errors in the nadir direction. A nadir pointing error of $\Delta\eta$ results in a mapping error on the ground of $\Delta\eta$*D/sinε where D is the slant distance to the ground and ε the elevation angle. This means that even when the payload is pointed vertically downward, an angular error equal to the iFOV will cause the payload's ground pixel to completely miss overlapping with ground pixels of the other satellites in the cluster. As the nadir pointing angle increases and elevation angle decreases, the mapping error gets worse and at 60° nadir pointing angle, an error of less than a fifth of iFOV causes a complete miss. An azimuthal pointing error of $\Delta\phi$ results in a mapping error on the ground of $\Delta\phi$*D*sinη where D is the slant distance to the ground and η the nadir pointing angle. However, since the cross track swath is multiple orders higher than the along track swath, probability of entirely missing the overlap is much lower. To overcome the above risks, HSI is a better choice than push broom imaging, that is, if we have 1000 spatial pixels, it is less risky to image a 20 X 50 spatial spot than a 1000 X 1 spatial vector.

   For a given number of pixels on the FPA, the swath variation is shown in Figure 15. Swath increases with altitude and with increased look angle. As expected, the maximum swath corresponds to near horizon viewing at the maximum satellite-target slant distance. The swath patterns for the FPI and AOTF type of spectrometer are nearly identical but very different from the WG spectrometer because the WGs image all the spectral bands of the 2D ground target at the same time onto the FPA while AOTFs/FPIs, being tuning filters, image the 2D target one band at a time, temporally. The actual number of spatial pixels available to the WG type, given a number of wavebands (nbands), is calculated in Equation 18. On the other hand, AOTFs are time constrained because each waveband has to be tuned into, imaged, integrated and read out within the time that the satellite flies to the next ground pixel so that image co-registration is not affected. The spatial pixels available for a given ground pixel size (gps), number of wavebands (nbands), readout time per pixel per image (readoutTime) and tuning time per waveband (tuningTime) is given by Equation 19. Equation 18 and Equation 19 demonstrate the different relationships between spatial and spectral ranges for the different spectral element types and therefore different effects on payload performance.

$$spatialPixelsWG = floor\left[\sqrt{\frac{totalPixels}{nbands}}\right]$$

Equation 18

$$intTime + nbands * [readoutTime * spatialPixelsAOTF + tuningTime] < \frac{gps}{V_g}$$

Equation 19

   At a typical rate of 1 megapixel per second, derived to maintain typical output circuit noise to below 5 electrons of noise equivalent signal for a 16 bit A/D, the readout time per pixel is 10^{-6}s and the tuning time per waveband is

10×10^{-6}s for AOTFs and 2×10^{-3}s for FPIs. For a ground speed of 7.2 km/s ($V_g = function(altitude)$), ground resolution of 500 m and 86 wavebands to be imaged, the maximum number spatial pixels available is 28X28 for a non-zero integration time. 28X28 pixels map to a swath between 5 and 12 km. If the number of required wavebands is reduced to 14 (minimum measurement requirement from the CAR instrument in Figure 3), at most 70X70 spatial pixels are available, mapping to a swath upto ~30 km. This demonstrates a clear trade-off between spatial and spectral range. The pixel numbers chosen for the AOTF trade in Figure 15 were therefore chosen as 50X50, 60X60 and 70X70 for 14 wavebands only to allow for enough range both spatially and spectrally. Equation 19, slightly modified, is applicable to WG spectrometers to calculate readout rates as well however it is required only once per exposure since all wavebands are imaged simultaneously, therefore eliminating any dependence on number of wavebands or tuning time seen in Equation 19. As a result, the spatial pixels available for the WGs are 1000, 1500 and 2000 per side distributed over 86 wavebands to be imaged.
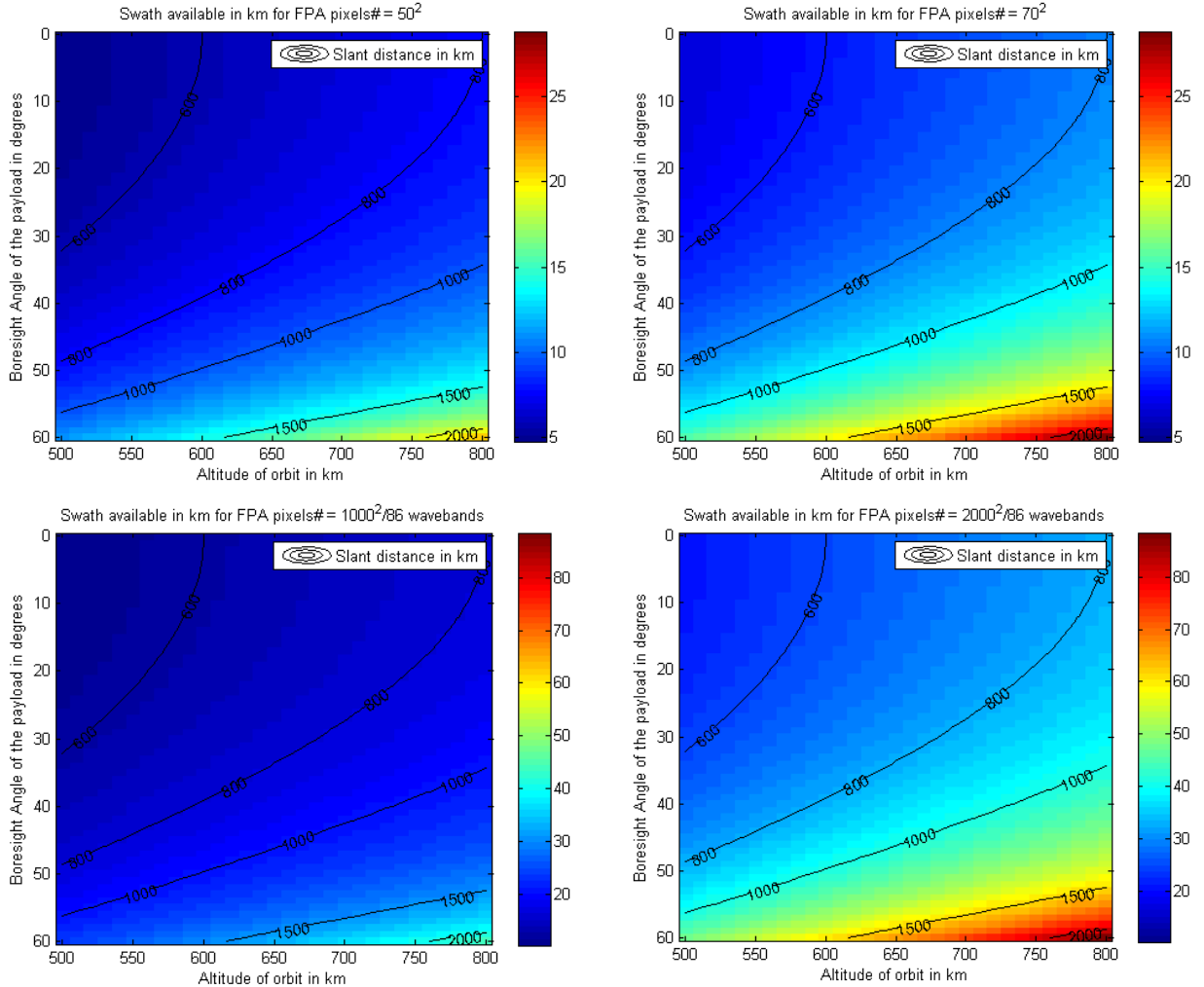

Figure 15: Simulated swath for an AOTF spectrometer (top row) and a WG spectrometer (bottom row) for a lower (left) and higher (right) number of pixels on the FPA – number marked on top - for varying boresight angles with respect to nadir and altitude. The total number of pixels on the WG FPA are shared between 86 spectral bands and actual spatial pixels. All the pixels on the AOTF FPA are available for spatial imaging because the spectral signal is extracted temporally. However, the total number of pixels for the AOTF spectrometer is severely restricted to allow for imaging and readout of all 14 (minimum requirement) spectral bands.

Total energy received by a 60X60 pixel FPA of the AOTF spectrometer is shown in Figure 16 and depends on the wavelength of light, solar zenith angle, altitude and nadir look angle. The tuning time for an AOTF is less than 10 μs (FPIs take <2 ms) so the time taken to tune to 14 spectral bands is < 1ms so the most time consuming

component that takes away from the integration time and therefore signal photos is the CCD readout time. The total signal is further restricted by the maximum number of spatial pixels that can be imaged in this limited time along with all 14 bands. A monotonic decrease in energy is seen in the visible range of light alone over nearly an order while about half an order of magnitude decrease is seen for a full range of change in the solar illumination angle. The power values at 1010 nm are chosen (from Figure 16's left panel) to demonstrate the variation of power with respect to altitude and boresight angle in Figure 16's right panel. The dependence on altitude is negligible compared to angles because COART's calculated radiance is barely affected by altitude above 100 km and slant height and therefore FOV varies far more due to look angle than orbit altitude. The minimal dependence on altitude will be seen in all charts that are a function of signal received.
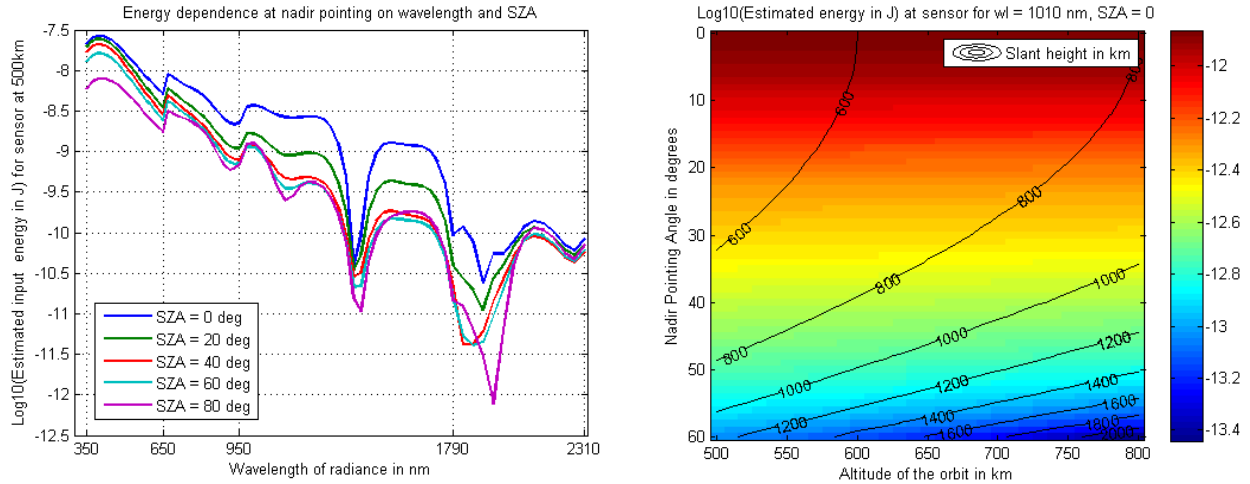

Figure 16: Simulated Energy that reaches the optical system of an AOTF spectrometer with 60X60 pixels as a function of wavelength and solar zenith angle for a nadir looking satellite at 500 km (left) and as a function of nadir/boresight pointing angle for a wavelength of 1010 nm at noontime. Contours mark the slant distance between the satellite and the ground target.

Simulated SNRs, calculated using Equation 12 and the associated noise values, for Waveguide and AOTF Spectrometers are shown in Figure 17. The former performs twice as well as the latter primarily due to larger number of spatial pixels and more integration time to accumulate signal photons. Both instruments show SNR>100 for all altitudes and view and solar zenith angles up until 1790 nm. The couple of hundred nanometers above 1790 nm correspond to the atmospheric block window therefore the signal is very low but returns to SNR>100 in the atmospheric window region again.

It is important to note that WGs image 86 bands in Figure 17 while AOTFs image only 14. AOTFs have a unique advantage in their tuning flexibility, that is, not all wavelengths need to be imaged like in a traditional spectrometer (e.g. waveguide FTS). The RF transducer can easily be programmed to skip the atmospheric block windows during spectral imaging which can save a significant fraction of the dwell time. This allows us to image more spatial pixels for greater integration times, therefore improving SNR. It is this tuning advantage that allows AOTFs to meet the minimum spectral requirements of BRDF science, as derived from the CAR instrument, without having to image the entire hyperspectrum. However, if a hyperspectrum is a mandatory BRDF application requirement, then WG spectrometers have a definite advantage both in swath covered and SNR.

To conclude this section, a trade-off between swath, SNR and number of image-able wavebands is quantified. These three payload system performance metrics identified in Figure 2 and Figure 4 are compared for the WG and AOTF spectrometers for a wavelength of 1010 nm, nadir viewing during noon from an altitude of 800 km. SNR (colorbar) and swath (contours) are plotted in Figure 18 against the required number of wavebands to be spectrally imaged and the required ground resolution of the spatial images.

For waveguide spectrometers (Figure 18 left panel), the number of spatial pixels available simply depends on the number of wavebands required (Equation 18), and that influences the swath imaged by a constant factor. The integration time available depends on the ground pixel size to dwell over, number of wavebands to image before integrating and number of pixels to read out after exposure (Equation 19), therefore SNR depends on all variables.

The total number of pixels on the FPA have been held constant at 1000X1000, therefore increasing wavebands decreases the number of spatial pixels available for imaging, which decreases the readout time required and increases the available integration time and therefore SNR.
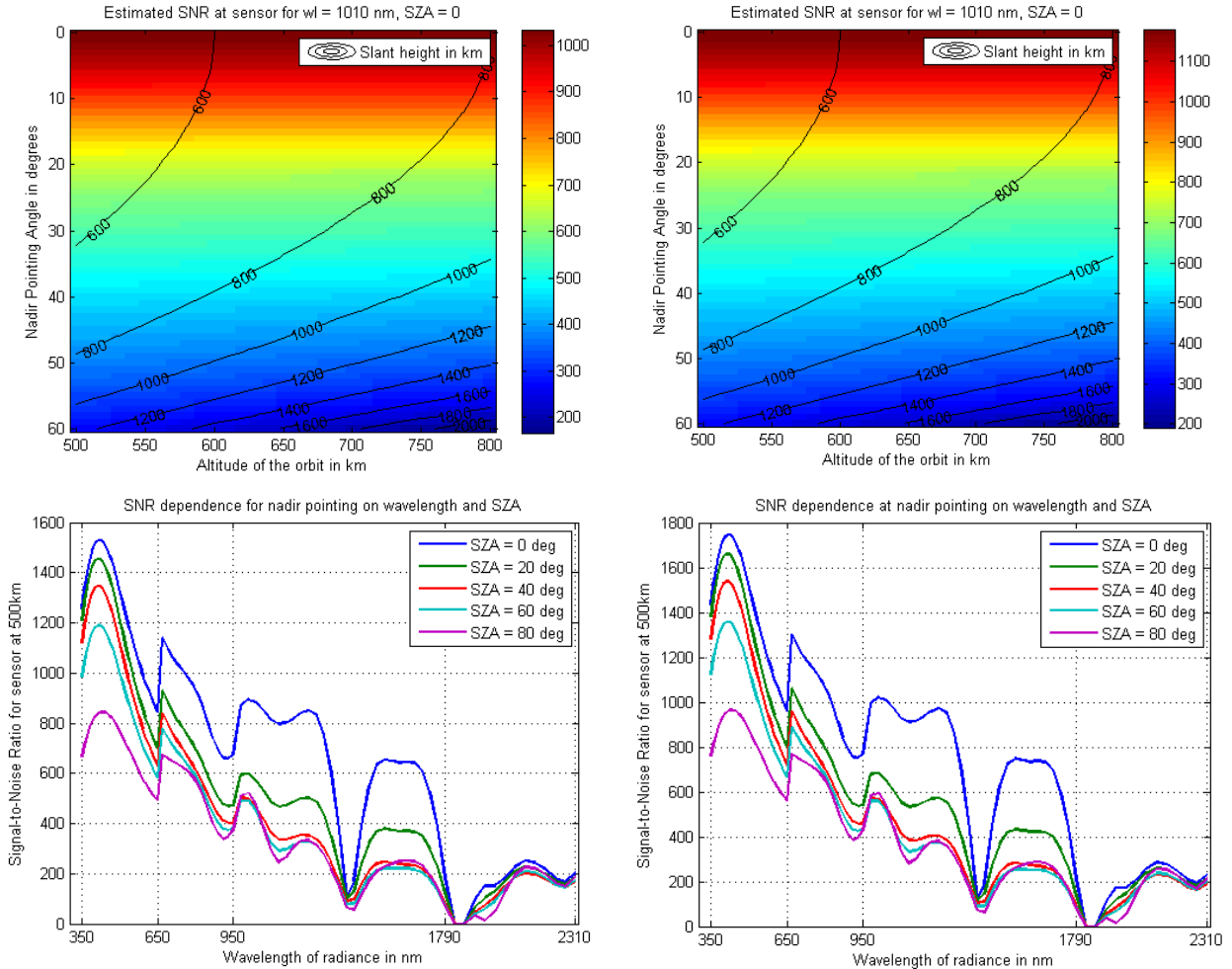

Figure 17: Simulated signal-to-noise ratios (SNR) for Waveguide Spectrometers with 1000X1000 FPA pixels (left) and AOTF spectrometers with 60X60 FPA pixels (right) as a function of nadir/boresight pointing angle for a wavelength of 1010 nm at noontime (top row) and as a function of wavelength and solar zenith angle, nadir viewing at a 500 km altitude. Quantum efficiency is assumed 0.5, charge transfer efficiency 0.8 and optical transmission 0.5. Contours mark the slant distance between the satellite and the ground target.

For AOTF spectrometers (Figure 18 right panel), the number of spatial pixels depends on all the variables considered (Equation 19) such that at least 5% of the total imaging time available is devoted as integration time while also maximizing spatial pixels. SNR is then dependent on the available integration time (IT in Equation 19) which influences SNR. The quantum jumps in the SNR chart are due to the constraint on spatial pixels to be integers only. The overall trend shows increased SNR with increased ground resolution required, as with WGs. However, by Equation 19, integration time and thus SNR increases (above at least 5% of the dwelling time) with decreasing wave numbers and ground resolution only up to the point where an extra spatial pixel can be fit in at which point the integration time quantum drops to 5% of the dwell time again. This causes the edge like pattern seen in the graph. Care must be taken to choose the number of spatial pixels carefully to avoid the design falling into a integration time minima.

It can clearly be seen that AOTFs achieve less than half the SNR and swath of WGs for the same number of wavebands. However, WGs have to image the spectrum continuously while AOTFs have the advantage of discontinuous spectral imaging and can meet the spectral requirements with lesser number of wavebands as well.
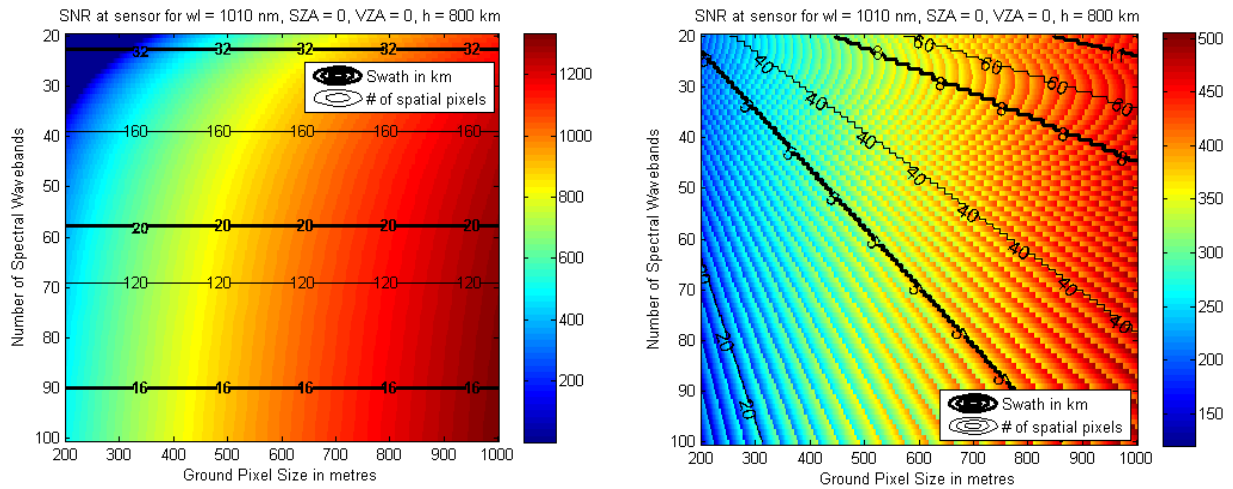
Figure 18: Simulated signal-to-noise ratios (SNR) for Waveguide Spectrometers (left) and Acousto-Optic Tunable Filters (right) as a function of spectral wavebands and ground resolution required to be imaged for a nadir looking satellite at 500 km, wavelength of 1010 nm and solar incidence at noon. The contours represent the achievable swath (thick black) and the effective number of spatial pixels available on the FPA (thin black), which is calculated dynamically to maximize swath while allowing at least 5% integration time for a given scenario.

The charts for FPIs are very similar to the AOTF, and the values within the same order of magnitude. The slight differences are attributed to the fact that the waveband switching time is 2 ms (compare to the tuning time of 10 μs for AOTFs). Therefore, the number of spatial pixels allowed for FPI imaging is slightly lesser than AOTFs. For example, a maximum of 55 spatial pixels would be possible to image instead of 70, causing the achievable swath of up to 20 km instead of 30 km (corresponding to Figure 15 top row). The SNRs are not affected much, and in fact, FPIs have SNR5-10 more. Overall, the performance of FPIs and AOTFs is similar with respect to the three metrics considered. The waveband number, ground resolution, wavelength and view geometry will be dictated by the geosciences application of multi-angle remote sensing. Nonetheless, SNR > 100 has been demonstrated to be achievable using available technologies within nanosatellite constraints for most ranges of the above variables.

IV.   Conclusions and Future Work

This paper identifies a critical Earth remote sensing application for hyperspectral snapshot imaging (HSI) and performs a feasibility study of nanosatellite HSI for this application. The application domain is called multi-angle, multi-spectral earth observation and BRDF is an important theoretical quantity thus estimated. BRDF is used to calculate important geosciences parameters such as gross primary productivity and snow albedo. Multiple copies of the instrument would be flown as the payload of multiple nanosatellites in formation flight or constellations. The presented work is a unique, systems-based approach to designing, customizing and evaluating a hyperspectral imager for these nanosatellites. It also presents a comprehensive and generalized tradespace analysis and optimization tool for payload design, customization and evaluation for any distributed space system mission (DSM).

For the multi-angle DSM application, external system requirements have been identified and quantified and payload system requirements as well as performance metrics calculated. Baseline optical parameters for NFOV payloads (diameter of 7 cm, focal length of 10.5 cm, pixel size of 20 μm) and technologies (HSI) are shown to lie within state-of-art and commercially affordable. The spectral elements shortlisted were WG Spectrometers, AOTFs, Electronically actuated FPIs and IFS. Qualitative evaluation favored AOTFs primarily because of their light weight, small size and flight heritage (TRL>6). However, quantitative analysis showed that WG spectrometers perform better in terms of achievable swath (10-90 km) and SNR (>100) for the same number of imaged wavebands. The different trade-offs between spatial and spectral range for the tuning versus waveguide spectrometers have been clearly quantified. AOTFs and FPIs (alike), being tunable filters, have the advantage of discontinuous spectral imaging and therefore can outperform WGs if only a few wavebands are needed or the atmospheric absorption bands need to be avoided. The better choice ultimately depends on the geosciences application within multi-angle imaging and the priorities of the listed metrics. This paper can be considered a feasibility study of using existing

23

technologies as payloads for nanosatellite HSI. Future work includes more detailed customization of the instrument in itself, in relation to other limiting systems in the nanosatellite such as attitude determination and control and communications and statistical analysis of noise, degradation and random processes that affect system performance.

V. Appendix: Calibration Methods

Calibration of the spectrometer will be required both pre-flight in the laboratory and also periodically in-flight.

Pre-flight calibration is best achieved using integrating spheres available within Goddard's airborne BRDF test facility [74]. The instruments used to calibrate include three integrating sphere sources (ISSs) operated at different light levels and experimental setups to determine radiance variability. The radiance gradients across the three ISS apertures were 0.2%–2.6% for different visible, near infrared and shortwave infrared illumination levels but 15% in the UV. Integrating spheres for laboratory calibration are now very well accepted and have been used in AVHRR, MODIS and MISR. Integrating spheres can be used for three types of tests:

1. Three integrating sphere sources (ISSs) are made to shine at different light levels as determined by the number of operating lamps—from 0–16 available lamps to ascertain linearity over the instrument performance range and to convert instrument digital counts into radiance units.
2. Measurement of the responsivity of the spectrometer (defined here as detector output per unit of incident power at a particular wavelength) at more than nine different distances from the ISS aperture to ascertain the sensitivity of calibration to distance of separation between the spectrometer and the ISSs
3. Determining the spectrometer responsivity across the mission angular range of 0 through 60°

The test data above is also used to determine [75] the dark noise of the spectrometer, the frame transfer offset (if an electric shutter is used and additional signals are accumulated when the frame is being transferred), saturation levels of the spectrometer and SNR and the spatial response uniformity of the signal over the detector pixels to show if the pixels have differential optical blur, spatial variation in optical element transmittance and pixel-to-pixel sensitivity differences.

In-flight calibration is more challenging especially in a small satellite with mass and power constraints. Calibration lamps were looked into in spite of their power requirement of <1W but were eliminated on the grounds of strict thermal requirements to keep the filament at a particular temperature. Additionally, the Hyperion spectrometer [76] demonstrated little dependence on lamp based calibration because of long-term instability (as large as 30% increase in the lamp's output) in spite of having an order of magnitude of more mass and power than small satellites. Acceptable calibration methods and their heritage include:

1. Calibration using white diffuser plates to reflect sunlight to the spectrometer as in VIIRS [77], MODIS and SELENE [78]. This will need precise knowledge of position and orientation with respect to the sun, a very stable internal diffuser and a mechanism (typically doors are used) to expose the spectrometer to the diffuser's signal instead of the earth and the need to calibrate during the day time. Spectralon [79–82] of the space-grade is found to be the best diffuser material because of its very high diffuse reflectance and Lambertian behavior. Roughened aluminum and Quazi Volume Diffuser, as used in the Ozone Mapping and Profiler Suite (OMPS), is an alternative to spectralon. While spectralon gets contaminated easily, the roughed Al has additional spectral features so there is a trade-off for either.
2. Lunar calibration by staring at the moon as in the SEVO payload in the O/OREOS spacecraft [83]. This requires precise phase and reflectance knowledge of the moon (the US Robotic Lunar Observatory (ROLO) database provides reliable numbers), can be conducted only at night and efficient calibration can be done only twice a month. The moon is a better candidate to stare at than the sun because the radiometric range of the sun is so large compared to the reflectance values the spectrometer is trying to measure that it will saturate the instrument
3. Vicarious calibration using ground control points of well known radiance at the BRDF angles and wavelengths such as the New Mexico or the Sahara desert. This can be done in the day and/or night, as shown in LandSat.

In-flight calibration checks the same quantities as laboratory calibration methods – responsivity, performance range, linearity, SNR, dark noise and spatial response uniformity. Depending on the attitude control capabilities of the nanosatellites, infrequent but periodic calibration maneuvers may also be planned [77]. These include rolls of different angles to acquire different images of the moon at different phases to track instrument radiometric degradation in the visible, near infrared, and shortwave infrared bands, yaw maneuvers over an angular range to perform a seasonal mapping of the radiometric performance of the on-board solar diffuser and a full pitch maneuver when the satellite is on the dark side to enable multiple scans of deep space to characterize non-solar infrared response.

VI. Acknowledgments

VII. References

1. Lyapustin, A. *et al.* Analysis of snow bidirectional reflectance from ARCTAS Spring-2008 Campaign. *Atmos Chem Phys* **10,** 4359–4375 (2010).
2. Liang, S. *Advances in land remote sensing: System, modelling, inversion and application*. (Springer, 2008).
3. Privette, J. L., Eck, T. F. & Deering, D. W. Estimating spectral albedo and nadir reflectance through inversion of simple BRDF models with AVHRR/MODIS-like data. *J. Geophys. Res.* **102,** 29529–29 (1997).
4. Esper, J., Neeck, S., Wiscombe, W., Ryschkewitsch, M. & Andary, J. Leonardo-BRDF: A New Generation Satellite Constellation. (2000). at <http://ntrs.nasa.gov/search.jsp?R=20000105058>
5. Gatebe, C. K. Airborne spectral measurements of surface–atmosphere anisotropy for several surfaces and ecosystems over southern Africa. *J. Geophys. Res.* **108,** (2003).
6. Nicodemus, F. E. *Geometrical considerations and nomenclature for reflectance*. **160,** (US Department of Commerce, National Bureau of Standards Washington, D. C, 1977).
7. Nag, S. Design of Nano-satellite Cluster Formations for Bi-Directional Reflectance Distribution Function (BRDF) Estimations. *AIAAUSU Conf. Small Satell.* (2013).
8. Barnsley, M. J., Strahler, A. H., Morris, K. P. & Muller, J. P. Sampling the surface bidirectional reflectance distribution function (BRDF): 1. Evaluation of current and future satellite sensors. *Remote Sens. Rev.* **8,** 271–311 (1994).
9. Xiong, X. *et al.* Terra and Aqua MODIS Design, Radiometry, and Geometry in Support of Land Remote Sensing. *Land Remote Sens. Glob. Environ. Change* 133–164 (2011).
10. Deschamps, P. Y. *et al.* The POLDER mission: Instrument characteristics and scientific objectives. *Geosci. Remote Sens. IEEE Trans.* **32,** 598–615 (1994).
11. Wielicki, B. A. *et al.* Clouds and the Earth's Radiant Energy System (CERES): An earth observing system experiment. *Bull. Am. Meteorol. Soc.* **77,** 853–868 (1996).
12. Diner, D. J. *et al.* Multi-angle Imaging SpectroRadiometer (MISR) instrument description and experiment overview. *Geosci. Remote Sens. IEEE Trans.* **36,** 1072–1087 (1998).
13. Godsalve, C. Bi-directional reflectance sampling by ATSR-2: a combined orbit and scan model. *Remote Sens.* **16,** 269–300 (1995).
14. Abrams, M. The Advanced Spaceborne Thermal Emission and Reflection Radiometer (ASTER): data products for the high spatial resolution imager on NASA's Terra platform. *Int. J. Remote Sens.* **21,** 847–859 (2000).
15. Barducci, A., Guzzi, D., Marcoionni, P. & Pippi, I. CHRIS-Proba performance evaluation: signal-to-noise ratio, instrument efficiency and data quality from acquisitions over San Rossore (Italy) test site. in *Proc. 3-Rd ESA CHRISProba Work. Italy* (2005).
16. O'Neill, M. G., Yue, H., Nag, S., Grogan, P. & de Weck, O. Comparing and Optimizing the DARPA System F6 Program Value-Centric Design Methodologies. in *Proc. AIAA Space Conf.* (2010).
17. Nag, S. & Summerer, L. Behaviour based, autonomous and distributed scatter manoeuvres for satellite swarms. *Acta Astronaut.* **82,** 95–109 (2013).
18. Nag, S., Gomez, E., Feller, S., Gibbs, J. & Hoffman, J. Laser communication system design for the Google Lunar X-Prize. in *Aerosp. Conf. 2011 IEEE* 1–20 (2011). doi:10.1109/AERO.2011.5747344
19. Nag, S., Hoffman, J. A. & de Weck, O. L. Collaborative and Educational Crowdsourcing of Spaceflight Software using SPHERES Zero Robotics. *Int. J. Space Technol. Manag. Innov. IJSTMI* **2,** 1–23 (2012).
20. Nag, S., Katz, J. G. & Saenz-Otero, A. Collaborative gaming and competition for CS-STEM education using SPHERES Zero Robotics. *Acta Astronaut.* **83,** 145–174 (2013).
21. Nag, S., Heffan, I., Saenz-Otero, A. & Lydon, M. SPHERES Zero Robotics software development: Lessons on crowdsourcing and collaborative competition. in *Aerosp. Conf. 2012 IEEE* 1–17 (2012).
22. Nag, S. Collaborative competition for crowdsourcing spaceflight software and STEM education using SPHERES Zero Robotics. (2012). at <http://dspace.mit.edu/handle/1721.1/78499>
23. Kramer, H. J. & Cracknell, A. P. An overview of small satellites in remote sensing*. *Int. J. Remote Sens.* **29,** 4285–4337 (2008).
24. Dyrud, L. *et al.* GEOScan: A global, real-time geoscience facility. in *Aerosp. Conf. 2013 IEEE* 1–13 (2013).

25. Okamoto, T. & Yamaguchi, I. Simultaneous acquisition of spectral image information. *Opt. Lett.* **16,** 1277–1279 (1991).
26. Okamoto, T., Takahashi, A. & Yamaguchi, I. Simultaneous Acquisition of Spectral and Spatial Intensity Distribution. *Appl. Spectrosc.* **47,** 1198–1202 (1993).
27. Bacon, R. *et al.* 3D spectrography at high spatial resolution. I. Concept and realization of the integral field spectrograph TIGER. *Astron. Astrophys. Suppl. Ser.* **113,** 347 (1995).
28. Mathews, S. A. Design and fabrication of a low-cost, multispectral imaging system. *Appl. Opt.* **47,** F71–F76 (2008).
29. Gupta, N., Ashe, P. R. & Tan, S. Miniature snapshot multispectral imager. *Opt. Eng.* **50,** 033203–033203 (2011).
30. Gorman, A., Fletcher-Holmes, D. W. & Harvey, A. R. Generalization of the Lyot filter and its application to snapshot spectral imaging. *Opt. Express* **18,** 5602–5608 (2010).
31. Vanderriest, C. Integral field spectroscopy with optical fibres. in *IAU Colloq 149 Tridimensional Opt. Spectrosc. Methods Astrophys.* **71,** 209 (1995).
32. Gata, N. *Imaging spectroscopy using tunable filters: A review*. **4056,** (Apr, 2000).
33. Blais-Ouellette, S., Daigle, O. & Taylor, K. The imaging Bragg tunable filter: a new path to integral field spectroscopy and narrow band imaging. in *Astron. Telesc. Instrum.* 62695H–62695H (2006).
34. Cheben, P. *Wavelength dispersive planar waveguide devices: echelle and arrayed waveguide gratings*. **5,** (chapter, 2007).
35. Georgiev, G., Glenar, D. A. & Hillman, J. J. Spectral characterization of acousto-optic filters used in imaging spectroscopy. *Appl. Opt.* **41,** 209–217 (2002).
36. Glenar, D. A., Hillman, J. J., Saif, B. & Bergstralh, J. Acousto-optic imaging spectropolarimetry for remote sensing. *Appl. Opt.* **33,** 7412–7424 (1994).
37. Hillman, J., Glenar, D., Kuehn, D. M. & Chanover, N. J. Compact Imaging Spectrometers using Acousto-Optic Tunable Filters. *Wkly. News Maganize Sci.* **155,** 26–30 (1999).
38. Saari, H. *et al.* Novel miniaturized hyperspectral sensor for UAV and space applications. in *SPIE Eur. Remote Sens.* 74741M–74741M (2009).
39. Mannila, R., Nasila, A., Praks, J., Saari, H. & Antila, J. Miniaturized spectral imager for Aalto-1 nanosatellite. in 817628–817628–8 (2011). doi:10.1117/12.897999
40. Fish, C., Marchant, A., Stromberg, E. & Sullivan, S. High Performance Spectroscopic Observation from a CubeSat. *AIAAUSU Conf. Small Satell.* (2013). at <http://digitalcommons.usu.edu/smallsat/2013/all2013/9>
41. Blackwell, W. *et al.* Nanosatellites for earth environmental monitoring: The MicroMAS project. in *Microw. Radiom. Remote Sens. Environ. MicroRad 2012 12th Spec. Meet.* 1–4 (2012).
42. Satori, S., Aoyanagi, Y., Hara, U., Mitsuhashi, R. & Takeuchi, Y. Hyperspectral sensor HSC3000 for nano-satellite TAIKI. in *Proc. SPIE Int. Soc. Opt. Eng.* 71490M–1 (2008).
43. Phong, L. N. & Ch^ateauneuf, F. Nanosatellite distributed far infrared radiometers. in *Proc SPIE* **7208,** 72080L (2009).
44. Mlynczak, M. G. *et al.* The Far-Infrared Detector Technology Advancement Partnership-FIDTAP. *Passive Opt. II* (2006). at <http://esto.nasa.gov/conferences/estc2006/papers/b5p2.pdf>
45. Alex Becerra, Marcos Diaz & J.C. Zagal. Feasibility study of using a Small Satellite constellation to forecast, monitor and mitigate natural and man-made disasters in Chile and similar developing countries.
46. S. Nag & O. L. de Weck. Nano-Satellite Clusters for Bi-Directional Reflectance Function (BRDF) Estimations. in *Proc. IAA Symp. Small Satell. Earth Obs.* (2013).
47. 65 Authors from the Astronautics Community. *Space Mission Engineering:The New SMAD*. (Microcosm Press, 2011).
48. Gino, M. C. Noise, noise, noise. *Httpwww Astrophys- Assist Comed. Htm* (2002).
49. Smith, M. W. *et al.* ExoplanetSat: detecting transiting exoplanets using a low-cost CubeSat platform. in *SPIE Astron. Telesc. Instrum. Obs. Front. Astron. New Decade* 773127–773127 (2010).
50. Cutter, M. A., Johns, L. S., Lobb, D. R., Williams, T. L. & Settle, J. J. Flight experience of the Compact High-Resolution Imaging Spectrometer(CHRIS). in *Proc. SPIE* **5159,** 392–405 (2003).
51. Green, R. O. *et al.* Imaging spectroscopy and the airborne visible/infrared imaging spectrometer (AVIRIS). *Remote Sens. Environ.* **65,** 227–248 (1998).
52. Stanton, E. J. & Puschell, J. J. Day/night band imager for a CubeSat. in *SPIE Opt. Eng. Appl.* 85160C–85160C (2012). at <http://proceedings.spiedigitallibrary.org/data/Conferences/SPIEP/69122/85160C.pdf>
53. Loewen, E. & Palmer, C. *Diffraction Grating Handbook*. (Newport Corporation, 2005).
54. Hewagama, Ti. *et al.* Miniature, Low-Power, Waveguide Based Infrared Fourier Transform Spectrometer for Spacecraft Remote Sensing. (2011). at <http://ntrs.nasa.gov/search.jsp?R=20110015229>

55. Fontaine, N. K., Okamoto, K., Su, T. & Yoo, S. J. B. Fourier-transform, integrated-optic spatial heterodyne spectrometer on a silica-based planar waveguide with 1?GHz resolution. *Opt. Lett.* **36,** 3124–3126 (2011).
56. Florjańczyk, M. *et al.* Spatial heterodyne planar waveguide spectrometer: theory and design. in *Proc SPIE* **7099,** 70991L (2008).
57. Rodrigo, J. A. *et al.* Fresnel diffraction effects in Fourier-transform arrayed waveguide grating spectrometer. *Opt. Express* **15,** 16431–16441 (2007).
58. Cheben, P., Powell, I., Janz, S. & Xu, D. X. Wavelength-dispersive device based on a Fourier-transform Michelson-type arrayed waveguide grating. *Opt. Lett.* **30,** 1824–1826 (2005).
59. Florjańczyk, M. *et al.* Planar waveguide spatial heterodyne spectrometer. in *Proc SPIE* **6796,** 67963J–1 (2007).
60. Okamoto, K. Progress and technical challenge for planar waveguide devices: silica and silicon waveguides. *Laser Photonics Rev.* **6,** 14–23 (2012).
61. Harlander, J. M. *et al.* Robust monolithic ultraviolet interferometer for the SHIMMER instrument on STPSat-1. *Appl. Opt.* **42,** 2829–2834 (2003).
62. Lin, Y. *et al.* Introduction to spatial heterodyne observations of water (SHOW) project and its instrument development. in *Proc XIV Int TOVS Study Conf* 25–31 (2005).
63. Chanover, N. J. *et al.* Probing Titan's lower atmosphere with acousto-optic tuning. *Icarus* **163,** 150–163 (2003).
64. Korablev, O. *et al.* An AOTF-based spectrometer for the studies of Mars atmosphere for Mars Express ESA mission. *Adv. Space Res.* **29,** 143–150 (2002).
65. Bertaux, J. L. *et al.* SPICAV on Venus Express: Three spectrometers to study the global structure and composition of the Venus atmosphere. *Planet. Space Sci.* **55,** 1673–1700 (2007).
66. Vila-Francés, J., Gómez-Chova, L., Amorós-López, J. & Calpe-Maravilla, J. Configurable Passband Imaging Spectrometer Based on Acousto-optic Tunable Filter. in *Proc. 10th Int. Conf. Adv. Concepts Intell. Vis. Syst.* 206–217 (Springer-Verlag, 2008). doi:10.1007/978-3-540-88458-3_19
67. Peters, M. A. *et al.* Conceptual design of the coronagraphic high angular resolution imaging spectrograph (charis) for the subaru telescope. in *SPIE Astron. Telesc. Instrum.* 84467U–84467U (2012).
68. M., P. A novel hyperspectral device without moving parts. in *Process. 7th Int. Conf. Space Opt.* (2008).
69. Jin, Z., Charlock, T. P., Rutledge, K., Stamnes, K. & Wang, Y. Analytical solution of radiative transfer in the coupled atmosphere-ocean system with a rough surface. *Appl. Opt.* **45,** 7443–7455 (2006).
70. Fraden, J. Handbook of Modern Sensors: Physics. *Des. Appl. Handb. Mod. Sensors SpringerVerlag* (2003).
71. Hoogeveen, R. W. M., van der A, R. J. & Goede, A. P. H. Extended wavelength InGaAs infrared (1.0–2.4 μm) detector arrays on SCIAMACHY for space-based spectrometry of the Earth atmosphere. *Infrared Phys. Technol.* **42,** 1–16 (2001).
72. McElwain, M. W. *et al.* Scientific design of a high contrast integral field spectrograph for the subaru telescope. in *Proc SPIE Vol* **8446,** 84469C–1 (2012).
73. Yuan, H. *et al.* FPA development: from InGaAs, InSb, to HgCdTe. in *Proc SPIE* **6940,** 69403C (2008).
74. Gatebe, C. K., Butler, J. J., Cooper, J. W., Kowalewski, M. & King, M. D. Characterization of errors in the use of integrating-sphere systems in the calibration of scanning radiometers. *Appl. Opt.* **46,** 7640–7651 (2007).
75. Kodama, S. *et al.* Characterization of Multiband Imager Aboard SELENE. *Space Sci. Rev.* **154,** 79–102 (2010).
76. Pearlman, J. S. *et al.* Hyperion, a space-based imaging spectrometer. *Geosci. Remote Sens. IEEE Trans.* **41,** 1160–1173 (2003).
77. Butler, J. J. *et al.* An overview of Suomi NPP VIIRS calibration maneuvers. in *SPIE Opt. Eng. Appl.* 85101J–85101J–13 (International Society for Optics and Photonics, 2012).
78. Ohtake, M. *et al.* Performance and scientific objectives of the SELENE (KAGUYA) Multiband Imager. *Earth Planets Space EPS* **60,** 257 (2008).
79. Bruegge, C., Chrien, N. & Haner, D. A Spectralon BRF data base for MISR calibration applications. *Remote Sens. Environ.* **77,** 354–366 (2001).
80. Bruegge, C. J., Stiegman, A. E., Rainen, R. A. & Springsteen, A. W. Use of Spectralon as a diffuse reflectance standard for in-flight calibration of earth-orbiting sensors. *Opt. Eng.* **32,** 805–814 (1993).
81. Courreges-Lacoste, G. B., Schaarsberg, J. G., Sprik, R. & Delwart, S. Modeling of Spectralon diffusers for radiometric calibration in remote sensing. *Opt. Eng.* **42,** 3600–3607 (2003).
82. Georgiev, G. T. & Butler, J. J. Long-term calibration monitoring of Spectralon diffusers BRDF in the air-ultraviolet. *Appl. Opt.* **46,** 7892–7899 (2007).
83. Minelli, G., Ricco, A. & Kitts, C. O. O/oreos nanosatellite: A multi-payload tech-nology demonstration. in *Proc. 24th Annu. AIAAUSU Conf. Small Satell.* (2010).